*Economic Geology,* v. 100, pp. 835–862

# Fluid Chemistry, Structural Setting, and Emplacement History of the Rosario Cu-Mo Porphyry and Cu-Ag-Au Epithermal Veins, Collahuasi District, Northern Chile

Glenton J. Masterman,[†,*] David R. Cooke, Ron F. Berry,

*Centre for Ore Deposit Research, University of Tasmania, Private Bag 79, Hobart, Tasmania 7001, Australia*

John L. Walshe,

*CSIRO Division of Exploration and Mining, P.O. Box 1130, Bentley, Western Australia 6102, Australia*

Andrew W. Lee,[**] and Alan H. Clark

*Department of Geological Sciences and Geological Engineering, Queens University, Kingston, Ontario, Canada K7L 3N6*

## Abstract

The Rosario Cu-Mo-Ag deposit is located in the Collahuasi district of northern Chile. It comprises high-grade Cu-Ag-(Au) epithermal veins, superimposed on the core of a porphyry Cu-Mo orebody. Rosario has mining reserves of 1,094 million metric tons (Mt) at 1.03 percent copper. An additional 1,022 Mt at 0.93 percent copper occurs in the district at the nearby Ujina and Quebrada Blanca porphyry deposits. The Rosario reserve contains over 95 percent hypogene ore, whereas supergene-sulfide ores dominate at Ujina and Quebrada Blanca.

Mineralized veins are hosted within Lower Permian volcanic and sedimentary rocks, Lower Triassic granodiorite and late Eocene porphyritic quartz-monzonite. The Rosario fault system, a series of moderate southwest-dipping faults, has localized high-grade Cu-Ag-(Au) veins. At Cerro La Grande, similar high-grade Cu-Ag-(Au) veins are hosted in north-northeast–trending, sinistral wrench faults. Normal movement in the Rosario fault system is interpreted to have been synchronous with sinistral strike-slip deformation at La Grande.

Hydrothermal alteration at Rosario is characterized by a K-feldspar core, focused in the Rosario Porphyry that grades out to a secondary biotite-albite-magnetite assemblage. Paragenetic relationships indicate that magnetite was the earliest formed alteration product but has been replaced by biotite-albite. Vein crosscutting relationships indicate that K-feldspar formed during and after biotite-albite alteration. Chalcopyrite and bornite were deposited in quartz veins associated with both K-feldspar and biotite-albite assemblages. The early hydrothermal fluid was a hypersaline brine (40–45 wt % NaCl) that coexisted with vapor between 400º and >600ºC. Weakly mineralized illite-chlorite (intermediate argillic) alteration of the early K and Na silicate assemblages was caused by moderate temperature (250º–350ºC), moderate-salinity brines (10–15 wt % NaCl). Molybdenite was precipitated in quartz veins that formed between the potassic and intermediate argillic alteration events. These fluids were 350º to 400ºC with salinities between 10 and 15 wt percent NaCl.

Porphyry-style ore and alteration minerals were overprinted by structurally controlled quartz-alunite-pyrite, pyrophyllite-dickite, and muscovite-quartz (phyllic) alteration assemblages. The quartz-alunite-pyrite alteration formed at 300º to 400ºC from fluids with a salinity of 10 wt percent NaCl. The pyrophyllite-dickite assemblage formed between 250º and 320ºC from dilute (5 wt % NaCl) fluids. An upward-flared zone of muscovite-quartz-pyrite altered rocks surrounds the fault-controlled domain of advanced argillic alteration. Thick veins (0.5–2 m wide) of fault-hosted massive pyrite, chalcopyrite, and bornite precipitated brines with a salinity of 30 wt percent NaCl at temperatures of 250º to 300ºC.

Pressure-depth estimates indicate that at least 1 km of rock was eroded at Rosario between formation of the K-Na silicate and advanced argillic assemblages. This erosion was rapid, occurring over a period of 1.8 m.y. The Rosario Porphyry intruded immediately after the Incaic tectonic phase, implying that it was emplaced as the Domeyko Cordillera underwent gravitational collapse, expressed as normal faults in the upper crust. Gravitational sliding potentially accelerated exhumation and helped to promote telescoping of the high-sulfidation environment onto the Rosario Porphyry.

The hydrothermal system responsible for porphyry Cu mineralization at Rosario was partially exhumed prior to the formation of high-sulfidation ore and alteration assemblages. This implies that emplacement of a second blind intrusion occurred somewhere beneath the Rosario and Cerro La Grande high-sulfidation vein systems and is supported by the fault geometry and zoning of precious metals and sulfosalts at the district scale.

## Introduction

Many porphyry copper deposits are associated with zones of advanced argillic alteration. Some of these alteration zones host high-sulfidation epithermal deposits (e.g., Lepanto-Far Southeast in the Philippines: Arribas et al., 1995; Hedenquist et al., 1998; La Mejicana-Nevados del Famatina, Argentina: Losada-Calderón, 1992; Losada-Calderón et al., 1994). The advanced argillic alteration assemblage typically forms at shallow crustal levels (200–1,000 m below the paleowater table: Arribas, 1995; Cooke and Simmons, 2000) in contrast to the zone of potassic alteration, which occurs at depths of ca.

[†] Corresponding author: e-mail, glen.masterman@bolnisigold.com.mx

[*] Current address: Bolnisi Gold NL, Calle Diego de Vilchis No 3503, Col. San Felipe C.P. 31240, Chihuahua, Chihuahua, Mexico.

[**] Current address: 24 Lyndale Drive, North York, Ontario, Canada M2N 2Y1.

0361-0128/05/3525/835-28 $6.00

1 to 3 km (Sillitoe, 2000). In northern Chile, several of the major Eocene-Oligocene porphyry Cu-Mo deposits are characterized by zones of advanced argillic alteration superimposed directly onto K silicate altered rocks. The best documented example occurs at Chuquicamata, where structurally controlled phyllic and advanced argillic alteration assemblages associated with Butte-style Cu-Ag veins (Sillitoe, 2000; Ossandon et al., 2001) have cut a broad zone of potassic alteration. Similar reversed zoning has been described in other Chilean porphyry Cu deposits, including Rosario (Dick et al., 1994; Lee, 1994), Mansa Mina (Sillitoe et al., 1996), La Escondida (Padilla Garza et al., 2001), and Quebrada Blanca (Hunt et al., 1983).

This study describes the temporal and spatial evolution of porphyry-related and high-sulfidation veins at the Rosario Cu-Mo-Ag deposit (Fig. 1). We also examine the structural controls on vein formation and use fluid inclusion microthermometry to estimate pressures during the main stage of vein formation. Exhumation rates during formation of porphyry and epithermal ore at Rosario have been constrained by the dating of early and late vein stages (Masterman et al., 2004). In this paper, we propose a scale-integrated structural and hydrothermal model to explain superpositioning of high-grade Cu-Ag massive sulfide veins onto low-grade porphyry Cu-Mo stockwork veins. Ore and alteration mineral assemblages and zoning in the late-stage massive sulfide veins are consistent with those described for high-sulfidation deposits by Hedenquist (1987), White and Hedenquist (1990, 1995), and Arribas (1995). Geodymanic implications for the formation of giant porphyry copper deposits in the north Chilean Andes are also discussed.

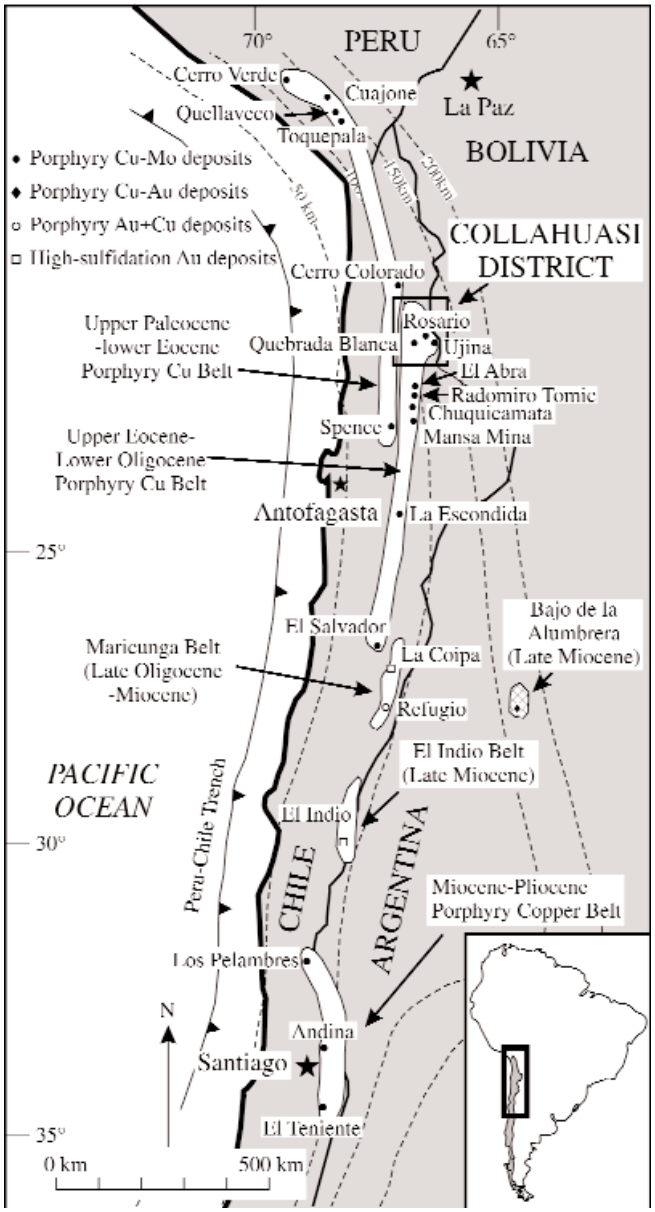


FIG. 1. Map showing the location of the Collahuasi district relative to other major copper and gold deposits in Chile and western Argentina. Metallogenic belts for the five major copper provinces are also shown. Dashed contour lines are the depths to the Wadati-Benioff zone. Modified from Muntean and Einaudi (2000).

## District and Deposit Geology

Collahuasi is situated in Region I of northern Chile, 5 to 10 km from the border with Bolivia (Figs. 1, 2). The geology of the Collahuasi district has been described by Vergara and Thomas (1984), Dick et al. (1994), Moore and Masterman (2002), and Masterman et al. (2004). The lowest stratigraphic units at Rosario comprise northeast-dipping volcanic and sedimentary rocks interfingered with graded feldspathic sandstone (Figs. 3, 4). These are conformably overlain by dacite ignimbrite (293 ± 14 Ma, U/Pb age: Masterman, 2003) interbedded with thick beds of tuffaceous sandstone, minor limestone (2–10 m thick), and rare units of coherent andesite (<5 m thick). Massive rhyodacite ignimbrite at the top of the sequence is concordant with the underlying stratigraphy (Fig. 3).

Copper mineralization at Rosario is associated with a series of northwest-trending quartz sulfide and massive sulfide veins occupying an area 1,500 m long and 1,200 m wide (Fig. 3). Ore-grade mineralization has been intersected to the current level of diamond drilling at depths of 900 m and is localized within and around a biotite porphyritic quartz-monzonite known as the Rosario Porphyry (C. Munchmeyer, J.P. Hunt, and H. Ware, 1984, Geología del Distrito de Collahuasi y del pórfido cuprífero Rosario: Santiago, Compañia Doña Inés de Collahuasi, Internal Company Report, p. 84; Dick et al., 1994; Lee, 1994) of late Eocene age (34.4 ± 0.4 Ma, $^{40}Ar/^{39}Ar$ primary biotite age: Masterman et al., 2004). This stock has intruded a porphyritic granodiorite called the Collahuasi Porphyry (245 ± 12 Ma: Masterman, 2003). Detailed descriptions of the Collahuasi and Rosario Porphyries are provided in Clark et al. (1998) and Masterman et al. (2004). The Collahuasi Porphyry is considerably older than any mineralization events at Rosario. Illite and alunite alteration at Rosario have been dated at 34.5 ± 0.5 and 32.6 ± 0.3 Ma, respectively ($^{40}Ar/^{39}Ar$ plateau ages: Masterman et al., 2004). Alunite at the La Grande epithermal vein system, 1.5 to 2 km south of Rosario (Fig. 2), formed at the same time as alunite at Rosario, based on a weighted mean plateau $^{40}Ar/^{39}Ar$ age of 32.7 ± 1.6 Ma (Masterman et al., 2004).

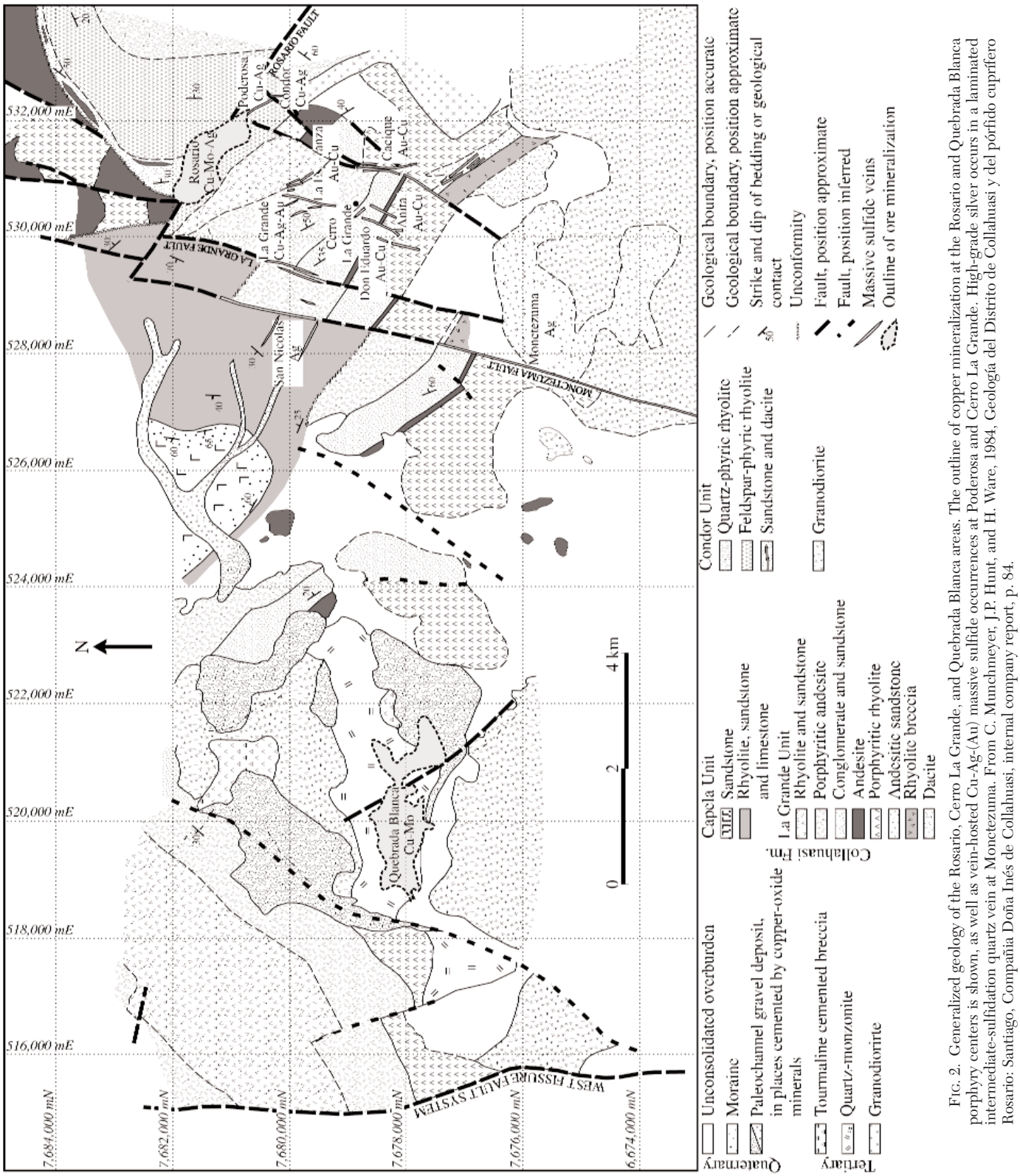


FIG. 2. Generalized geology of the Rosario, Cerro La Grande, and Quebrada Blanca areas. The outline of copper mineralization at the Rosario and Quebrada Blanca porphyry centers is shown, as well as vein-hosted Cu-Ag-(Au) massive sulfide occurrences at Poderosa and Cerro La Grande. High-grade silver occurs in a laminated intermediate-sulfidation quartz vein at Moctezuma. From C. Munchmeyer, J.P. Hunt, and H. Ware, 1984, Geología del Distrito de Collahuasi y del pórfido cuprífero Rosario: Santiago, Compañía Doña Inés de Collahuasi, internal company report, p. 84.

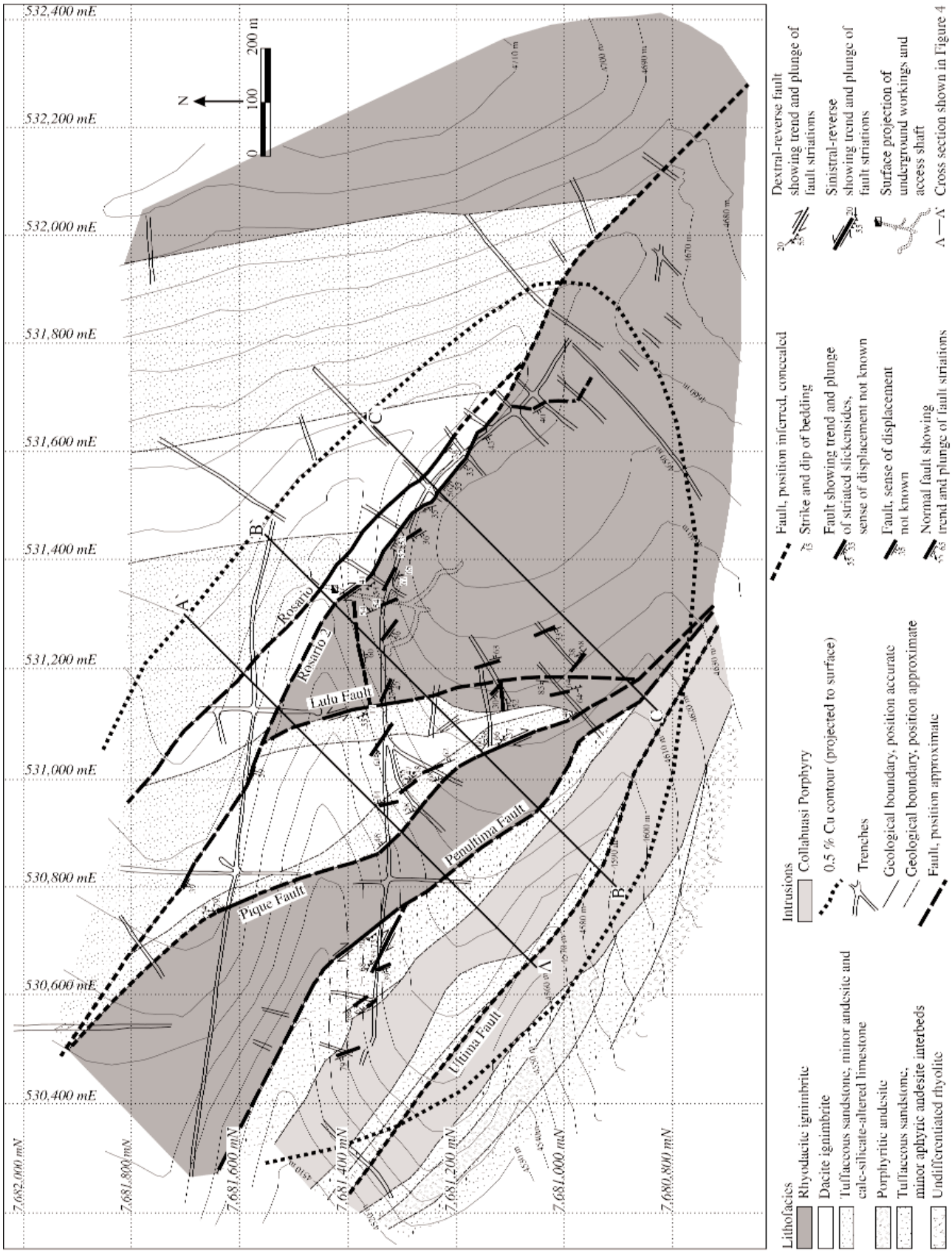


FIG. 3. Interpreted solid geology of the Rosario deposit based on 1:2000 surface mapping and 1:200 graphic logging of diamond drill core. Surface rock exposure was generally limited to costeans and rare outcrops on hill slopes. The trajectories and dips of geologic contacts and major faults were projected along strike between trench crosscuts. Fault kinematic indicators, where measured, are shown with apparent stratigraphic displacements reflecting the most recent movement history.

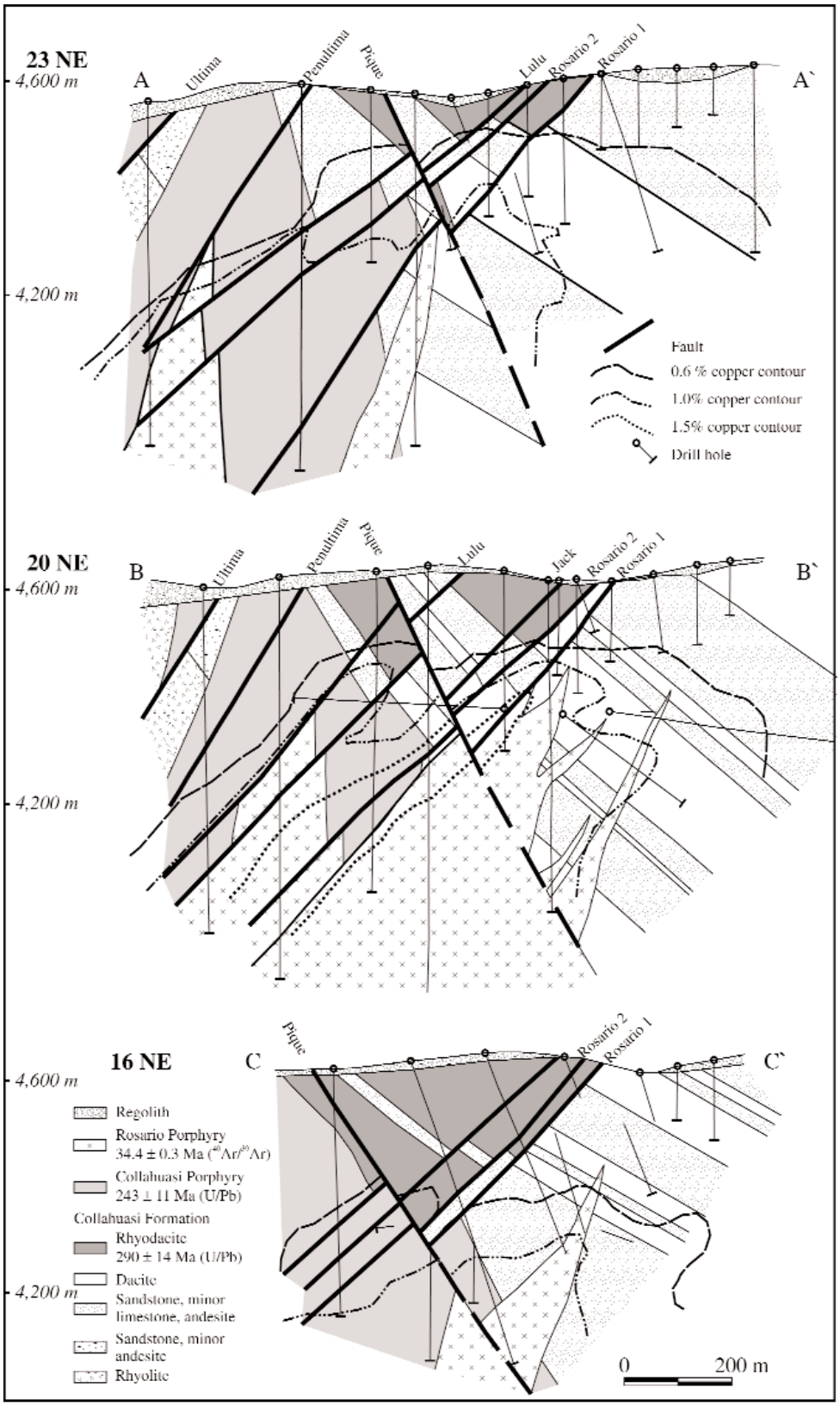


FIG. 4. Stacked northeast-southwest geologic sections through the Rosario deposit. Surface traces of each section are shown in Figure 3. Contours of hypogene copper grades are shown at the 0.6, 1.0, and 1.5 percent levels. The highest copper grades (>1.5% Cu) occur in the late-stage veins associated with the southwest-dipping Rosario fault system. The 1 percent Cu contour closely follows the outline of the Rosario Porphyry. Geologic interpretations are based on drill hole logging completed in this study and Masterman et al. (2004). Names refer to faults.

The Collahuasi district contains two major copper-molybdenum porphyry deposits in addition to Rosario, which were not included in our structural study. The Ujina deposit is located approximately 7 km southeast of Rosario and has been dated at 35.2 ± 0.3 Ma ($^{40}Ar/^{39}Ar$ primary biotite age: Masterman et al., 2004). The Quebrada Blanca deposit, located 8 km southwest of Rosario (Fig. 2), has an age similar to that of Ujina, based on a $^{40}Ar/^{39}Ar$ age determination on secondary biotite (34.9 ± 0.4 Ma: Maksaev, 1990). These deposits formed prior to the emplacement of the giant Rosario porphyry and associated La Grande veins, which appear to mark the culmination of mineralization within the district.

## Structure

In the Rosario and La Grande areas, development of brittle faults postdated folding in the Collahuasi Formation. A series of moderate to steep (45°–65°), southwest- and northeast-dipping faults (the Rosario fault system) have cut the orebody (Figs. 3, 4) and are associated with advanced argillic alteration and high-grade, polymetallic Cu-Ag-(Au) veins. These faults show considerable dextral (up to 1,100-m strike separation) and minor sinistral (300-m strike separation) offsets (Fig. 3). A second group of faults, striking north-northeast, occur in the Cerro La Grande area 2 to 4 km south of Rosario (Fig. 2). These faults also contain high-grade polymetallic Cu-Ag-(Au) veins (Dick et al., 1994; Lee, 1994).

### *Fault evolution*

Two discrete fault reactivation events have been identified from detailed analysis of kinematic indicators on the major fault surfaces using the techniques outlined in Petit (1987) and Doblas (1998). First generation striations, characterized by steep-pitching grooves on polished surfaces, are associated with normal faults (Fig. 5A). Paleostress modeling, using the method of Etchecopar et al. (1981), indicates that normal faulting occurred under near-vertical maximum compressive stress ($\sigma_1$) and southwest-trending subhorizontal minimum compressive stress ($\sigma_3$). This marks the first phase of brittle deformation during which the Rosario fault system is interpreted to have formed as a series of synthetic and antithetic extensional faults.

At Rosario, the only major fault with sinistral strike-slip movement is the Lulú fault (figs. 3, 5B). This fault has been truncated by dextral displacement in the Rosario 2 and Pique faults. The sinistral Monctezuma and La Grande faults also have been dextrally offset by the Rosario fault system (Fig. 2). Left-lateral deformation in the Lulu, Monctezuma, La Grande, and Cacique faults may have occurred before, during, or after normal movement in the Rosario fault system.

A second generation of subhorizontal striations (Fig. 5C) is associated with dextral strike-slip reactivation evident in the dextral strike separation of volcanic facies on either side of both faults. Dextral strike-slip kinematic indicators have been directly observed in the Penúltima fault and are implied by the apparent dextral displacement of the Collahuasi Porphyry along the Ultima fault (Fig. 3). The maximum compressive stress ($\sigma_1$) during brittle dextral strike-slip deformation was near horizontal, trending 160° during dextral strike-slip deformation (Fig. 5C).

### *Paleostress fields*

Evolution of the local paleostress field at Rosario is shown in Figure 6. Stress tensors modeled for the sinistral faults are consistent with those derived from kinematic data on the normal faults (Fig. 6). Moreover, both fault systems host high-grade polymetallic Cu-Ag-(Au) veins. We infer that left-lateral movement in the north-northeast–trending faults was synchronous with normal movement in the Rosario fault system and that high-sulfidation mineralization formed at this time. Mineralization predated dextral-reverse reactivation of these faults, based on observed fault textures in the massive sulfide veins, including sigmoidal tension gashes and sulfidic clast-supported microbreccias (Masterman, 2003). We further infer that the minimum compressive stress ($\sigma_3$) during formation of these faults was northeast directed and permitted southwest escape in the Rosario fault system and left-lateral displacement along the north-northeast–trending faults at Cerro La Grande (Fig. 6A).

The local stress field during postmineralization dextral reactivation of the Rosario fault system is shown in Figure 6B. The model shows that the principal compressive stress directions were rotated clockwise relative to the stress field

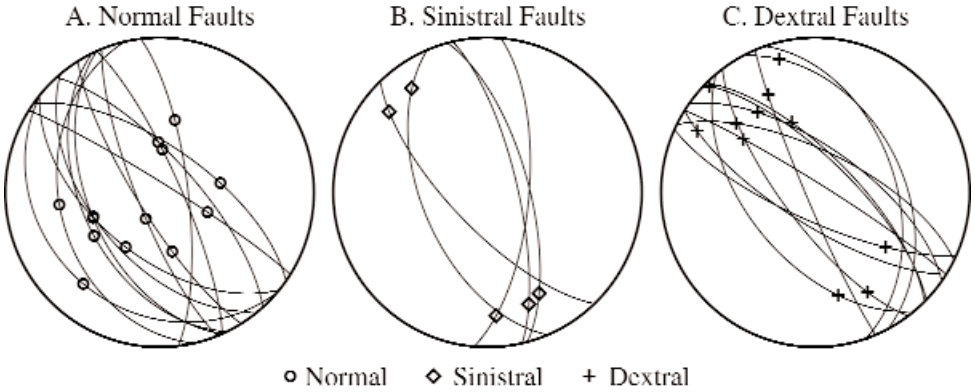


FIG. 5. Lower hemisphere equal area projections of major faults at Rosario. Symbols in the great circles are trend and plunge of fault striations. A. Normal faults. B. Sinistral faults. C. Dextral faults. Reactivation of normal faults during dextral strike-slip movement is supported by overlapping fault orientations and overprinting striations on fault surfaces. The north-northwest orientation of sinistral faults is consistent with the interpretation that they accommodated southwest escape during normal faulting.

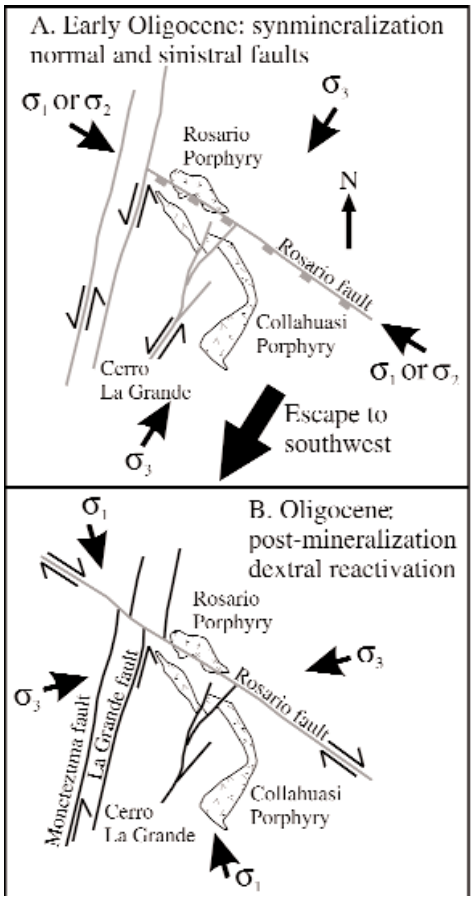


FIG. 6. Schematic model for the local paleostress field and brittle deformation-reactivation in the Rosario and La Grande areas. Faults colored gray are the active faults. A. Formation of high-grade Cu-Ag-(Au) veins in normal faults at Rosario and sinistral faults at Cerro La Grande in the early Oligocene. Paleostress modeling indicates that compression was directed locally to the southeast, with escape to the southwest parallel to the direction of $\sigma_3$. B. Postmineralization dextral reactivation of the Rosario fault system. Clockwise rotation of $\sigma_1$ to north-northwest resulted in dextral movement in the northwest-trending faults at Rosario. There also may have been some sinistral reactivation of the north-northeast–trending faults.

responsible for normal and sinistral movement. However the calculations of Etchecopar et al. (1981) used in the paleostress modeling assume that the fracture patterns are propagated in cohesive rock. Therefore, the amount of rotation of the local stress field required to reactivate the Rosario fault system as dextral faults was probably less than that indicated in Figure 6B.

## Mineral Mapping

Zones of ore and alteration mineral associations were mapped in detail across three northeast-southwest vertical cross sections at the Rosario deposit (Fig. 7) and a single east-west section through the La Grande vein (Fig. 8). Drill core logging was augmented by a short-wave infrared absorption (SWIR) spectroscopic study that identified fine-grained alteration minerals. In total, 19 drill holes at Rosario (7,470 m) and two at La Grande (1,100 m) were logged graphically. Rock type, structure, vein types and paragenesis, relative ages of intrusions, ore and alteration mineral associations and their distribution, and approximate volume percent of the main mineral constituents were recorded. SWIR spectra obtained using an Integrated Spectronics Pty. Ltd. portable infrared microanalyzer (PIMA) were collected on 1,046 diamond drill core samples. Detailed examination of sulfide and alteration overprinting relationships was carried out on 120 polished thin sections using transmitted and reflected light microscopy.

Spectra were obtained on zones of bleached alteration every 4 m to evaluate small-scale mineralogical variations through zones of clay and white mica alteration. Sample spacing was 8 to 16 m in zones of hydrothermal alteration that lacked white micas and clay (e.g., biotite or chlorite altered rocks). Multiple spots were analyzed by the PIMA in each core sample following the procedure of Thompson et al. (1999). Mineral identification was made by comparing each measured spectrum to a reference database using The Spectral Geologist processing software (AUSSPEC International Pty. Ltd). Spectral mineral identification was confirmed by detailed petrographic examination of the altered rocks, as well as electron microprobe analyses, which was used to determine fine-scale compositional variations in individual minerals.

## Veins and Altered Rocks

The spatial and temporal distribution of veins and associated alteration, based on crosscutting relationships and mineral overprinting textures, is illustrated in Figure 9 and summarized in Table 1. We use the A, B, and D vein nomenclature of Gustafson and Hunt (1975), the C vein nomenclature of Dilles and Einaudi (1992), and the M vein nomenclature of Arancibia and Clark (1996) to describe the main vein types recognized at Rosario. Seven vein stages (M, A-1, A-2, A-3, B, C, and D veins) are related to porphyry-style ore and alteration types, of which there are four distinct alteration assemblages. These assemblages include magnetite, biotite-albite, K-feldspar, and illite-chlorite (Figs. 7, 9). About 50 percent of the copper at Rosario is associated with the early A-stage veins, with another 10 to 20 percent in the B- and C-stage veins (Fig. 9). Most of the molybdenite occurs in B veins.

Fault-hosted polymetallic massive sulfides, defined as E veins in this study, is the last vein type to have formed at Rosario (Fig. 9). The E veins are characterized by two main infilling stages. The first consists of pyrite, chalcopyrite, bornite, and chalcocite and is associated with an alteration assemblage of quartz-alunite ± diaspore ± andalusite ± barite. The second is the tennantite-enargite stage (TES), which also contains minor mawsonite, colusite, and vinciennite. The tennantite-enargite stage is associated with pyrophyllite-dickite alteration proximal to veins and phyllic (muscovite) grading out to argillic (illite-smectite) alteration assemblages away from veins. The pyrophyllite-dickite alteration assemblage has overprinted the earlier formed assemblage of quartz-alunite-pyrite. Muscovite-quartz and illite-smectite alteration of the wall rocks is interpreted to have formed contemporaneously with the pyrophyllite-dickite assemblage (Fig. 9). These late-stage veins account for about 30 to 40 percent of the total copper at Rosario.

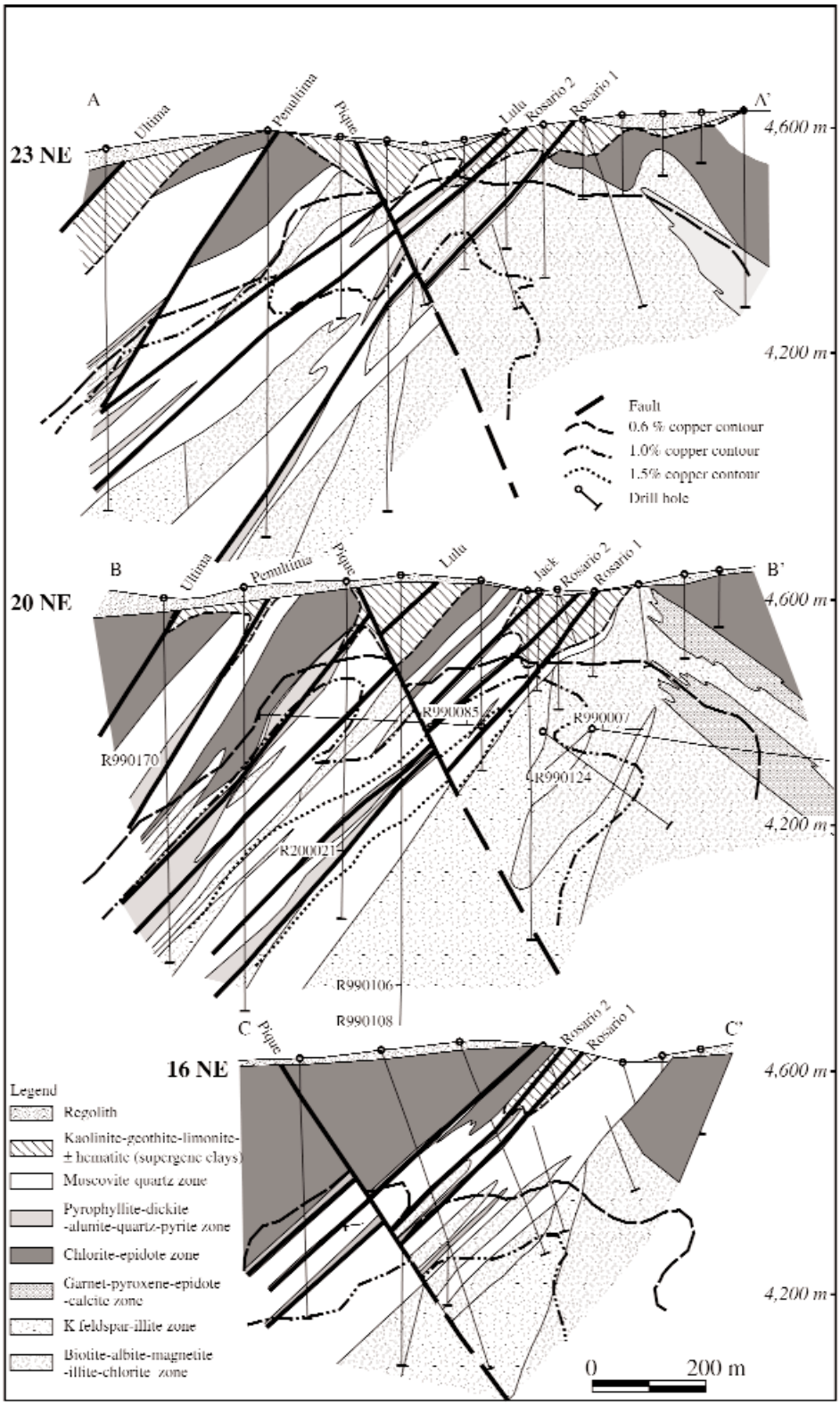


FIG. 7. Stacked northeast-southwest alteration sections in the Rosario deposit (see Figs. 3 and 4 for locations). All sections have the same coordinates in the northeast section lines. Contours of hypogene copper grades are shown at the 0.6, 1.0, and 1.5 wt percent Cu values. The Rosario fault system controls pyrophyllite-rich alteration that grades out to muscovite fringed by zones of kaolinite-illite-smectite. K-feldspar alteration in the core of the deposit is enveloped by biotite-magnetite-albite alteration. Chlorite-epidote alteration surrounds all other alteration types on the margins of the deposit. Section B-B' is reproduced from Masterman et al. (2004). Fluid inclusion sample localities are indicated by the numbers R990007, R990124, R990106, R990108, R990085, 990170, and R200021.

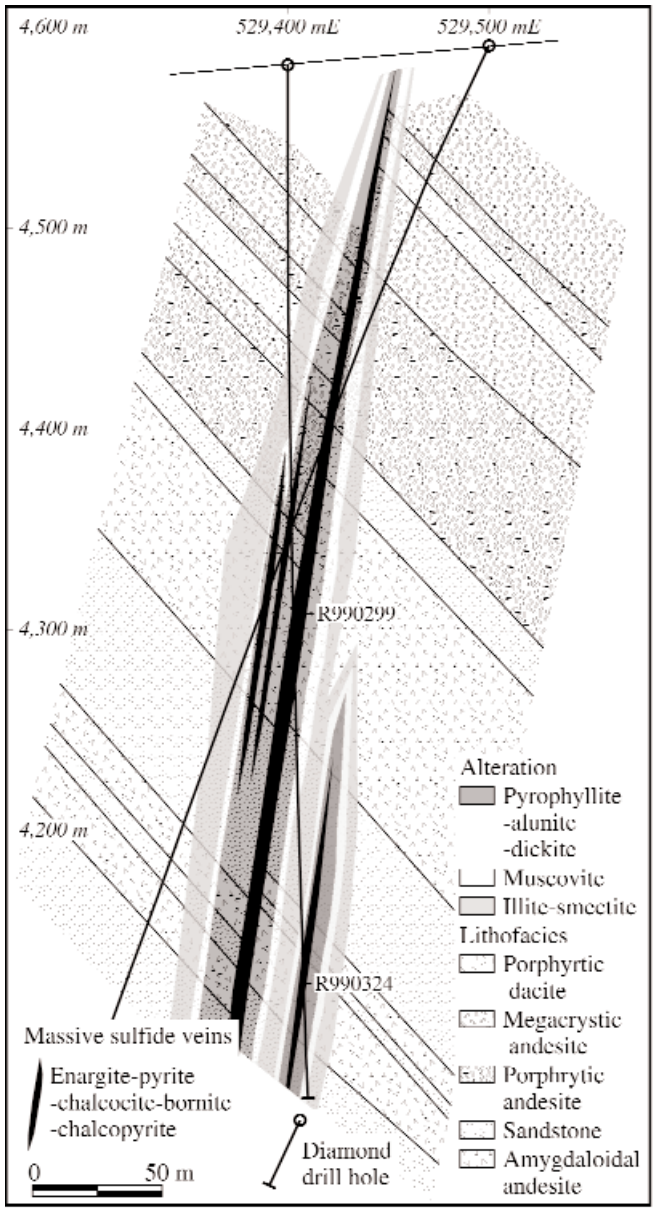


FIG. 8. East-west cross section through the La Grande veins. The subvertical veins cut coherent volcanic rocks, interbedded with thick (10–50 m) sedimentary units. The rocks dip 40° NE. Amygdaloidal andesite interbedded with crystal-sandstone at the bottom of the sequence is overlain by porphyritic and megacrystic andesite and porphyritic dacite. Hydrothermal alteration of the wall rocks is typically restricted to a zone, 25 m wide, on opposite sides of the vein but reaches 50 m wide in the amygdaloidal andesite. Alteration zoning is characterized by pyrophyllite-alunite-dickite next to the vein, surrounded by muscovite that grades out to an illite-smectite fringe. The volcanic rocks are altered to epidote-chlorite beyond the zone of illite-smectite alteration. Vein minerals are pyrite, enargite, chalcocite, and bornite. The vein has a maximum thickness of 15 m and averages 30 wt percent Cu, 70 g/t Ag, and 0.8 g/t Au. Fluid inclusion sample localities are indicated by the numbers R990299 and R990324.

### *M veinlets*

Irregular, discontinuous magnetite (M) veinlets occur only in the Permo-Triassic host rocks that surround the Rosario Porphyry. They are generally <0.3 mm wide and are the earliest vein type seen in the Rosario deposit. M veinlets comprise chains and beads of magnetite (Fig. 10A). The veinlets lack definitive walls and have no internal structure. M veinlets are interpreted to have formed, in part, by replacement of wall rock because there is no evidence of open-space filling. No M veinlets were observed in the Rosario Porphyry.

### *A-1 and A-2 veinlets*

Irregular and segmented A-1 veinlets contain biotite, minor quartz, and chalcopyrite. Quartz-albite-biotite A-2 veinlets are discontinuous, range from <0.3 to 5 mm wide, have sharp irregular walls, and contain minor chalcopyrite, pyrite, rutile, and magnetite (Fig. 10B). Both of these vein types occur in the biotite-albite-magnetite-illite-chlorite alteration zone (Fig. 7). The alteration halos that surround A1 veins are, in places, indistinguishable from the strongly developed ragged biotite that occurs as a background alteration assemblage. By contrast, A-2 veins have well-defined albite halos, stained brown by the presence of fine-grained biotite. Secondary albite in these halos has replaced primary plagioclase in contact with the veinlets. A-1 veinlets are locally cut by A-2 veinlets. Both vein types cut M veinlets. A-1 and A-2 veinlets are concentrated in the volcanic and sedimentary host rocks but are rare in the Rosario Porphyry.

### *A-3 veinlets and veins*

K-feldspar–bearing A-3 veins have cut M, A-1, and A-2 veinlets and are most abundant in the Rosario Porphyry. Chalcopyrite and bornite are the main ore minerals in these veins. A-3 veins are 5 mm to 2 cm wide and exhibit either irregular, discontinuous, and segmented walls or regular, continuous, and parallel walls. Alteration envelopes associated with A-3 veins are easily recognized in rocks that lack pervasive secondary K-feldspar, as their pink K-feldspar halos are clearly distinguishable. The envelopes are generally 2 mm to 5 cm wide and comprise perthitic K-feldspar and minor chalcopyrite and bornite. Pervasive K-feldspar altered rock is spatially associated with high densities of A-3 veins, evident in a few drill holes at depths greater than 600 m below surface (Fig. 10C).

### *B veins*

B veins are continuous planar fractures, with parallel walls that have been filled by anhedral to subhedral quartz and minor K-feldspar. Some B veins contain parallel lateral bands of flaky molybdenite intergrown with granular quartz. Molybdenite more typically occurs in vein selvages, together with anhedral quartz and K-feldspar (Fig. 11A-B). B veins generally lack alteration envelopes.

In some B veins, anhedral quartz has been overgrown by euhedral quartz, and central voids have been filled by chalcopyrite and/or pyrite (Fig. 11B). Both types of quartz contain fluid inclusions and show undulose extinction, with minor subgrain development on grain boundaries. Some chalcopyrite and pyrite grains in the veins contain inclusions of molybdenite, whereas others have truncated molybdenite grain boundaries. B veins with euhedral quartz and chalcopyrite-pyrite filling the centers of the veins are typically associated with texturally destructive, fine-grained muscovite envelopes.

### *C veins*

C veins have regular, continuous walls, some internal banding, and vary from <3 mm to 2 cm wide. C veins cut B veins,

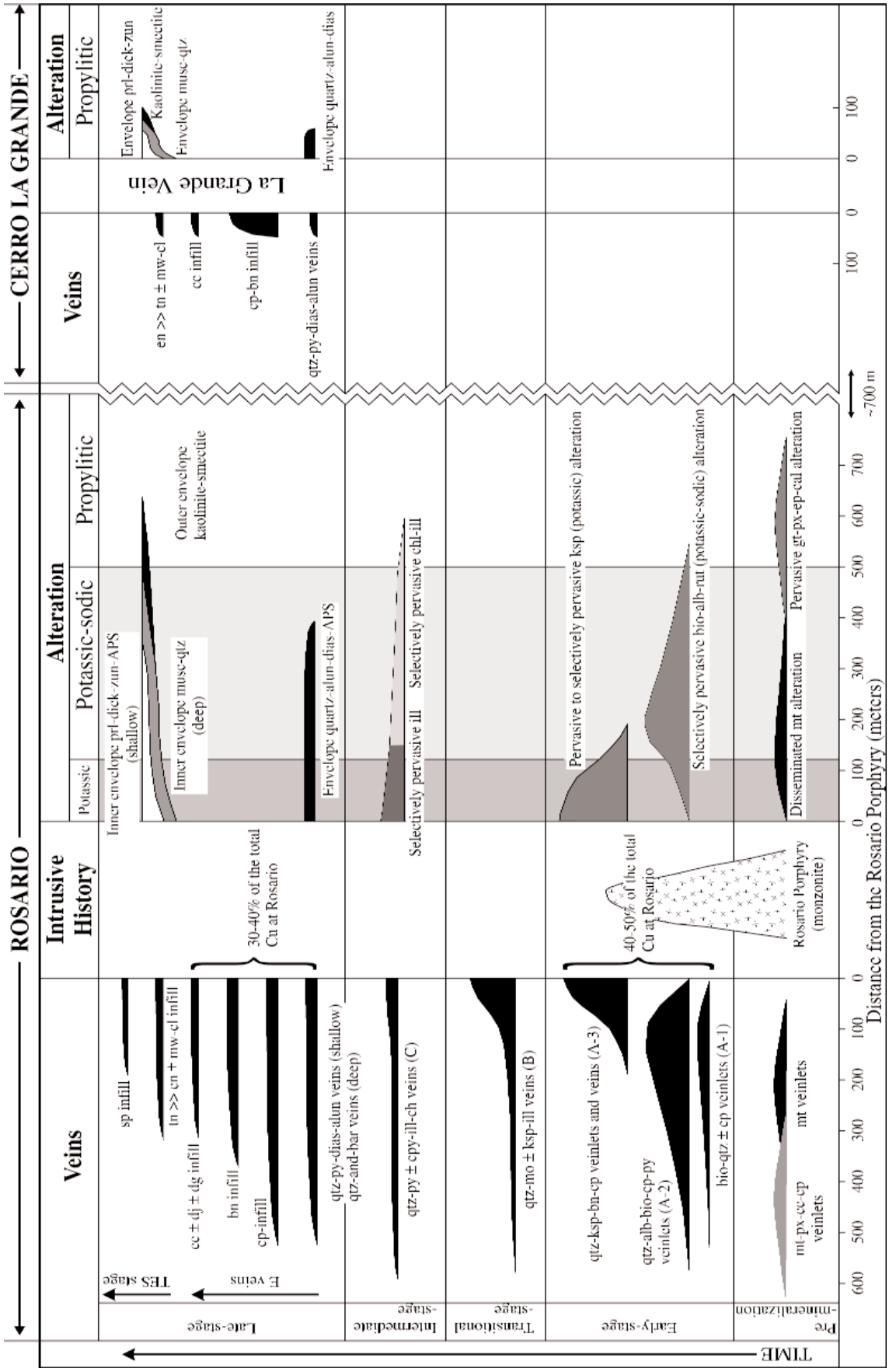


FIG. 9. Schematic time-space diagram showing the vein and alteration paragenesis in the Rosario and La Grande deposits. The earliest events are at the bottom of the diagram The length of the bars show the lateral distribution of vein development or an alteration assemblage relative to the Rosario Porphyry. In the late-stage veins, sulfide paragenesis is shown as a series of vein infilling stages. Vein and alteration paragenesis is based on crosscutting and overprinting relationships observed in drill core and detailed petrography. Rock abbreviations: PCO = Collahuasi Porphyry, PRO = Rosario Porphyry. Mineral abbreviations: alb = albite, alun = alunite, and = andalusite, APS = aluminum-phosphorous-sulfate minerals, bar = barite, bio = biotite, bn = bornite, cal = calcite, cc = chalcocite, chl = chlorite, cl = colusite, cp = chalcopyrite, dg = digenite, dias = diaspore, dick = dickite, dj = djurleite, en = enargite, ep = epidote, gar = garnet, ill = illite, ka = kaolinite, ksp = K-feldspar, mo = molybdenite, mt = magnetite, musc = muscovite, mw = mawsonite, prl = pyrophyllite, px = pyroxene, py = pyrite, qtz = quartz, rut = rutile, sp = sphalerite, tn = tennantite, vin = vinciennite, zun = zunyite.

TABLE 1. Summary of Vein Type and Attendant Alteration Listed in Sequence from Oldest to Youngest

| Vein type | Distribution | Vein textures | Vein infilling | | | | | | Wall-rock alteration halo | | |
|---|---|---|---|---|---|---|---|---|---|---|---|
| | | | Major | | Minor | | | | | | |
| | | | Gangue | Opaque | Gangue | Opaque | Thickness | Structure | Major | Minor | Thickness |
| M veinlets (as defined by Arancibia and Clark, 1996) | | | | | | | | | | | |
| 1. Mt | Moderately abundant in country rock, absent in the Rosario Porphyry | Chains and/or beads | - | Mt | Alb, qtz, bio, chl | Cp, rut | <0.3 mm | No wall definition | - | - | - |
| A veins and/or veinlets (as defined by Gustafson and Hunt, 1975) | | | | | | | | | | | |
| 2. Bio-qtz | Abundant in country rock, rare in the Rosario Porphyry | Wavy, discontinuous | Bio | - | Qtz, chl | Cp, rut | <0.3 mm | Irregular walls | - | - | - |
| 3. Qtz-alb-bio-cp-py | Moderately abundant in country rock proximal to the Rosario Porphyry, rare in the Rosario Porphyry and distal country rock | Anhedral, granular qtz | Qtz-alb-bio | Cp, py | Ksp, chl | Mt, rut | <5.0 mm | Irregular, nonparallel walls, no internal symmetry | Alb | Bio, ksp, chl, rut | <2 mm |
| 4. Qtz-ksp-cp-bn | Abundant in the Rosario Porphyry, moderately abundant in country rock proximal to the Rosario Porphyry | Anhedral, granular quartz | Qtz, ksp | Cp, bn | Bio, | Rut | <2.0 cm | Irregular-regular walls, lack internal symmetry | Ksp | Bio, ill, rut | <2 mm |
| B veins (as defined by Gustafson and Hunt, 1975) | | | | | | | | | | | |
| 5 Qtz-mo | Abundant in and proximal to the Rosario Porphyry | Subhedral to euhedral quartz, flaky molybdenite | Qtz | Mo | Ksp, ill, chl | Py, rut | Generally 1–3 cm, up to 15 cm | Regular walls | - | Ksp, ill, chl, qtz | <1 cm |
| C veins (as defined by Dilles and Einaudi, 1992) | | | | | | | | | | | |
| 6. Qtz-cp-py-ill-chl | Moderately abundant throughout the Rosario Porphyry and country rock | Subhedral to euhedral quartz | Qtz | Cp, py | Ill, chl | Rut | <3.0 mm | Regular walls | Ill, chl, qtz | Py, rut | <2 cm |
| D veins (as defined by Gustafson and Hunt, 1975) | | | | | | | | | | | |
| 7. Py-cpy | Most abundant in structurally controlled zone of muscovite alteration | Semimassive sulfide, euhedral quartz | - | Py, cp | Mu, qtz | Rut | <1.0 cm | Regular walls | Mu, qtz | Chl | <10 cm |
| E veins (this study) | | | | | | | | | | | |
| 8. Py-bn-cpy-cc-dj-dg | Major polymetallic veins occur in strands of the Rosario fault system, subsidiary veinlets occur with qtz-alun-dias gangue and alteration envelopes | Massive sulfide | - | Py, bn, cp | Qtz, alun, bar, APS, zun | Cc, dj, dg, | Centimeters to meters | Regular walls | Qtz, alun, dias | Zun, APS, rut | Centimeters to meters |
| Tennantite-enargite stage (TES; this study) | | | | | | | | | | | |
| 9. Tn > en (Rosario), (La Grande) | Cut the E vein py-bn-cpy assemblage, associated with prl-dick altered rock proximal to vein, musc-qtz altered rock distal to veins and deep | Massive sulfide | Qtz | Tn, en | Prl, dick, APS, zun, musc, bar, and | Mw, col, vin, sp | Centimeters | Late-stage infilling in E and new veins | Prl, dick, musc | APS, zun, bar, and | Centimeters to meters |

- = no data

Mineral abbreviations: alb = albite, alun = alunite, and = andalusite, APS = aluminium-phosphorous-sulfate minerals, bar = barite, bio = biotite, bn = bornite, cal = calcite, cc = chalcocite, chl = chlorite, col = colusite, cp = chalcopyrite, dg = digenite, dias = diaspore, dick = dickite, dj = djurleite, en = enargite, ep = epidote, gar = garnet, ill = illite, ka = kaolinite, ksp = K-feldspar, mo = molybdenite, mt = magnetite, mw = mawsonite, prl = pyrophyllite, py = pyrite, qtz = quartz, rut = rutile, sl = sphalerite, tn = tennantite, vin = vinciennite, zun = zunyite

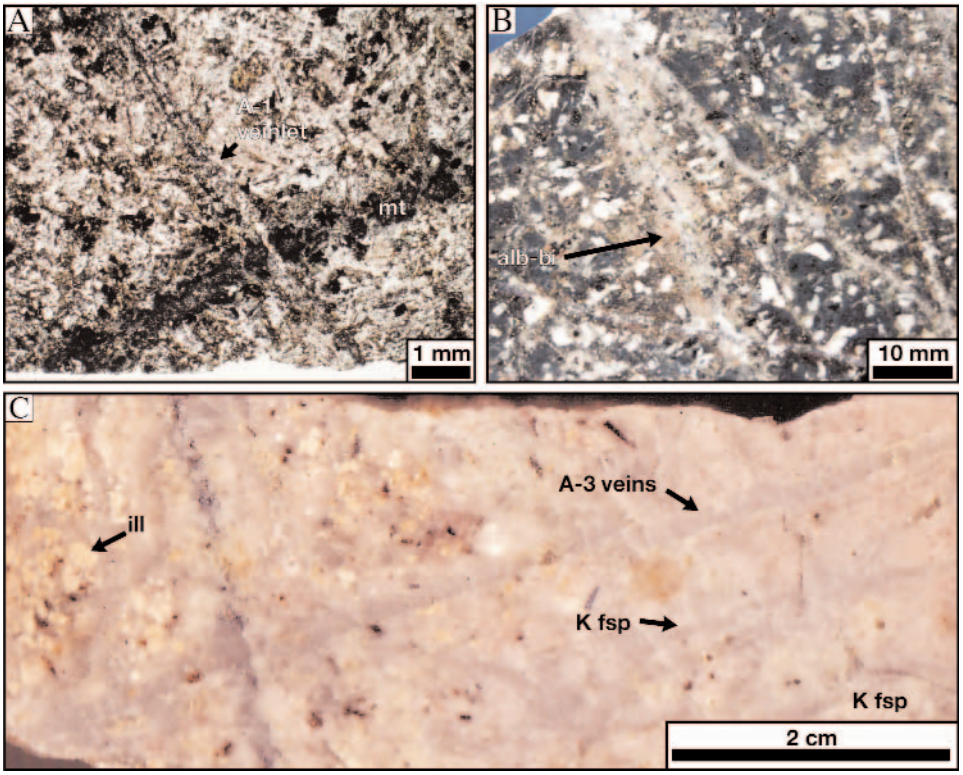


FIG. 10. Photographs and photomicrographs of magnetite M and A veins from zones of biotite-magnetite-albite and K-feldspar alteration. A. Photomicrograph of a biotite-quartz-chalcopyrite A-1 vein that cuts a magnetite vein in biotite-magnetite-albite altered porphyritic andesite (plane-polarized light). B. Photograph of biotite-, magnetite-albite-chlorite-illite altered porphyritic dacite. Dark clots disseminated through the rock are biotite-magnetite-chlorite intergrowths. The cores of feldspar phenocrysts have been replaced by illite. The rock is cut by several generations of A-2 veins. The light brown stain in the bleached envelopes of the vein is due to the presence of biotite inclusions in secondary albite. C. Example of pervasive K-feldspar alteration in the Rosario Porphyry. Note that the porphyritic texture has been destroyed in the rock on the right-hand side of the sample. This zone corresponds with a high density of quartz-K-feldspar-bornite-chalcopyrite A-3 veins. On the left-hand side, phenocrysts have been enhanced by illite replacement of the feldspar. M and A vein nomenclature from Arancibia and Clark (1996) and Gustafson and Hunt (1975), respectively. Abbreviations: alb = albite, bi = biotite, ill = illite, K fsp = K-feldspar, mt = magnetite.

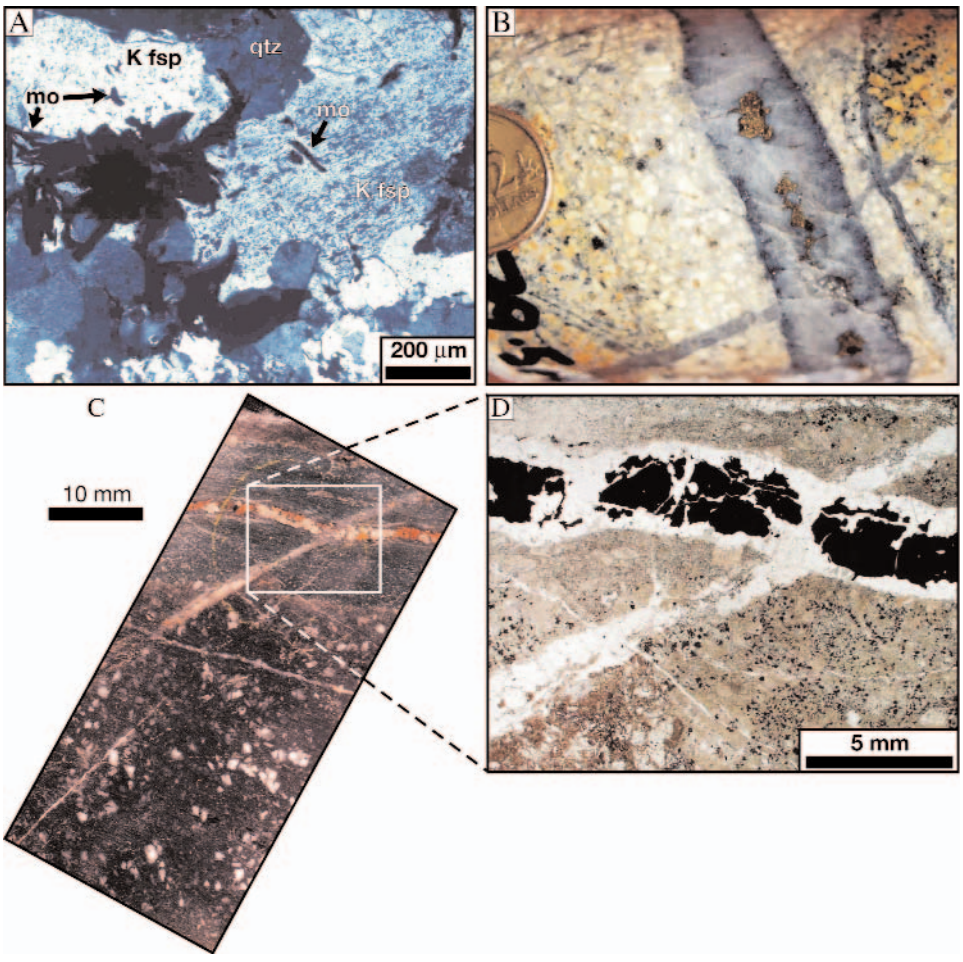


FIG. 11. Photographs and photomicrographs of B and C veins. A. Photomicrograph of flaky molybdenite inclusions in K-feldspar. Molybdenite and K-feldspar are associated with subhedral quartz and chalcopyrite in the vein selvage (cross-polarized light). B. Photograph of drill core from the Rosario Porphyry. In this example, the quartz-chalcopyrite-molybdenite B vein cuts the quartz-K-feldspar-chalcopyrite veins. Flaky molybdenite is associated with anhedral to subhedral quartz in the vein selvage, whereas chalcopyrite occupies the central part of the vein. Phenocryst shapes in the bleached envelope of the vein consist entirely of muscovite. Bleached phenocrysts outside the envelope are illite. Coin diameter = 20 mm. C. Photograph of biotite-magnetite-albite altered andesite cut by a pyrite-chalcopyrite-quartz C vein with a chlorite-illite alteration envelope. D. Inset from C. Photomicrograph of the vein and alteration envelope. Note that the chlorite-illite envelope around the late vein overprints the ragged biotite envelope around the early vein (plane-polarized light). B and C vein nomenclature from Gustafson and Hunt (1975) and Dilles and Einaudi (1992), respectively. Abbreviations: K fsp = K-feldspar, mo = molybdenite, qtz = quartz.

A veins, and M veinlets. They occur throughout the K-feldspar-illite and biotite-albite-magnetite-illite-chlorite alteration zones. The veins are filled with quartz, pyrite, and minor chalcopyrite, illite, and chlorite. Quartz is typically euhedral with crystals grown perpendicularly to the vein walls and distributed symmetrically on both sides of the vein. Quartz prisms attached to vein walls terminate in central domains now filled by pyrite and chalcopyrite. C vein envelopes contain chlorite and minor illite, which are best developed in the biotite-albite-magnetite-illite-chlorite alteration zone (Fig. 11C-D).

*D veins*

These are planar and continuous veins of pyrite with subordinate quartz, muscovite, and chalcopyrite. They typically occur parallel to the orientation of the Rosario fault system (Fig. 7). D veins are less than 1 mm to more than 20 cm wide and cut M, A, B, and C veins in all alteration zones. Pyrite is the principal vein mineral, with minor chalcopyrite. Euhedral quartz, present in some veins, shows undulose extinction and contains abundant fluid inclusions. D veins have muscovite alteration halos. In the biotite-albite-magnetite-illite-chlorite alteration zone, the alteration halos are zoned outward from feldspar-destructive muscovite through muscovite-chlorite to chlorite.

*E veins*

Polymetallic massive sulfide (E) veins have cut all other veins, except for some D veins at Rosario. The widest E veins (0.5–5 m) occur in branches of the Rosario fault system (Fig. 7). Smaller veins (0.5–10 cm) are concentrated near the faults but decrease in abundance away from these zones. The main sulfides in E veins are pyrite, chalcopyrite, bornite, chalcocite, tennantite, and enargite (Fig. 12A-B). Gangue minerals, which constitute up to 20 vol percent of veins, include quartz, alunite, diaspore and zunyite ± andalusite, barite, and pyrophyllite. Vein alunite, which occurs as euhedral blades, contains anhedral inclusions of diaspore and APS minerals (Fig. 12C-D).

*Tennantite-enargite stage (TES)*

Tennantite (Fig. 12A-B) and enargite occur generally as replacements of pyrite, bornite, chalcopyrite, and chalcocite within E veins at Rosario. Minor Sn-bearing sulfides, including mawsonite, colusite, and vinciennite also overprint bornite, chalcocite, and chalcopyrite and have formed contemporaneously with tennantite and enargite (Fig. 12B). Microfractures (<50 $\mu$m wide) that have cut bornite and chalcopyrite are lined by djurleite and digenite with sphalerite in centers of the fractures.

*Structural controls on vein formation at Rosario*

Structural analysis of vein orientations, based on detailed underground mapping by Lee (1994), revealed that most vein types have a preferred orientation parallel to the Rosario fault system. Early-formed A veins in the Rosario Porphyry and adjacent to the Rosario fault have no apparent preferred orientation (Fig. 13A), although this interpretation may change if there were more data. By contrast, B veins have a preferred orientation of 320°/77° SW, occurring in high densities near the Rosario 1 and 2 faults (Fig. 13B). Late-stage E and tennantite-enargite stage veins occur in southwest- and northeast-dipping conjugate populations (339°/65 SW and 321°/50 NE, respectively; Fig. 13C). The bisecting angle between the two averaged populations of the late-stage E veins is ~65°, consistent with subvertical $\sigma_1$ and subhorizontal southwest $\sigma_3$ estimated in the paleostress model for normal faulting at Rosario (Fig. 6A).

*The La Grande veins*

Subvertical massive sulfide veins occur in the northeast-dipping volcanic units at La Grande (Fig. 8), 1.5 km southwest of Rosario. These volcanic rocks occur stratigraphically below those that host the Rosario deposit. Narrow alteration envelopes (10–15 m wide) in volcanic rocks surrounding the veins are zoned outward from inner pyrophyllite-dickite-quartz-diaspore-alunite (±APS minerals)-zunyite out through muscovite and illite-smectite assemblages to outer chlorite-epidote.

The La Grande veins are 0.5 to 15 m wide, with smaller veins (1–20 cm wide) typically restricted to pyrophyllite alteration envelopes (<20 m wide). Enargite, pyrite, chalcocite, and bornite are the main sulfides (Fig. 12E), with subordinate colusite and mawsonite. The main La Grande vein lacks gangue, but the small veins contain up to 50 vol percent quartz, dickite, zunyite, pyrophyllite, and minor APS minerals, with or without alunite (Fig. 12F). The sulfide paragenesis in the La Grande veins is the same as in the Rosario E veins. Enargite constitutes the bulk of the sulfide assemblage and has overprinted all other copper-bearing sulfides. Colusite and mawsonite appear to have formed contemporaneously with enargite.

*District-scale metal zonation*

The precious and base metal sulfide mineral assemblages within E veins are zoned between Rosario and Cerro La Grande (Fig. 14). Historically, major veins in Cerro La Grande were mined for Cu and Au. Vein samples from the Don Eduardo, Forastera, and Anita workings, 2 to 3 km south of Rosario, have Ag/Au values between 25/1 and 5/1 (Platt, 1988). By comparison, the Poderosa veins located 500 m southeast of Rosario were mined predominantly for Cu and Ag with Ag/Au values of 65/1 (C. Munchmeyer, J.P. Hunt, and H. Ware, 1984, Geología del Distrito de Collahuasi y del pórfido cuprífero Rosario: Santiago, Compañia Doña Inés de Collahuasi, Internal Company Report, p. 84). Typically, the E veins are enargite rich at Cerro La Grande and tennantite rich at Rosario (Fig. 14). Sphalerite is present in E veins at Rosario but has not been observed in veins around Cerro La Grande.

## Fluid Inclusions

A reconnaissance study of fluid inclusions was carried out to assess the spatial and temporal evolution of hydrothermal fluids at Rosario and La Grande. Quartz containing workable fluid inclusions was sampled from diamond drill core. A total of 21 doubly polished wafers (150 $\mu$m thick) were examined petrographically, including samples from each vein stage. Ten wafers were selected for heating and freezing measurements. These samples have provided information

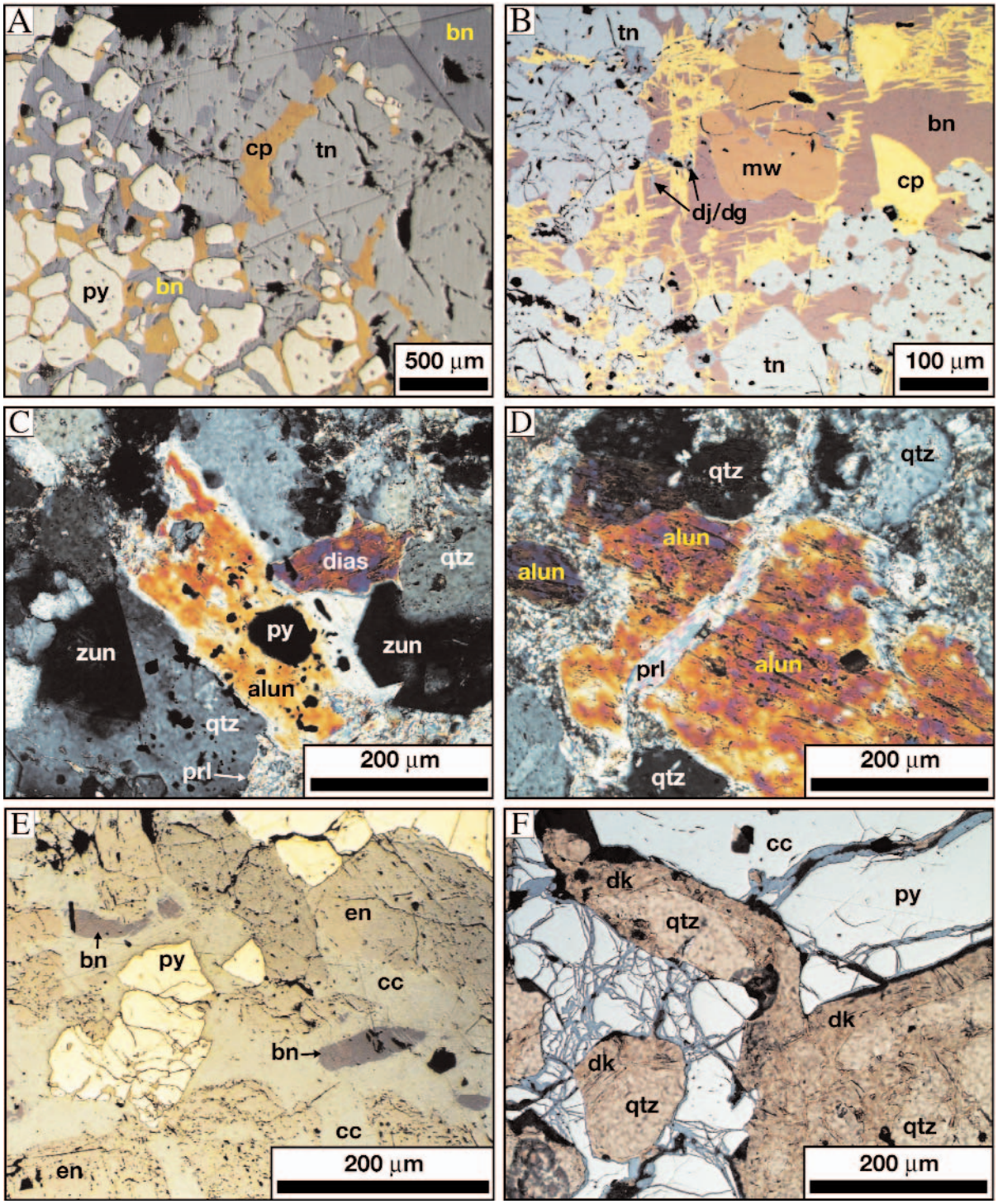


FIG. 12. A. Photomicrographs of pyrite, tennantite, bornite, and chalcopyrite in an E vein from Rosario (reflected light). Scale bar = 500 $\mu$m. B. Photomicrographs of partial tennantite-mawsonite (tennantite-enargite stage) replacement of bornite and chalcopyrite (reflected light). C. Photomicrograph of the Collahuasi Porphyry overprinted by pervasive quartz-diaspore-alunite-± pyrophyllite-zunyite. The isotropic crystal with cubic habit is zunyite (cross-polarized light). D. Photomicrograph of a pyrophyllite veinlet that has cut tabular alunite (cross-polarized light). E. Photomicrograph of E vein massive sulfides in the La Grande vein. Enargite coexists with pyrite, chalcocite, and bornite (reflected light). F. Photomicrograph of euhedral quartz and pyrite. The pyrite has been cut by chalcocite-filled veinlets. Chalcocite also has overgrown quartz. Platy dickite occurs around the margins of the euhedral quartz against the pyrite and truncates the veinlets of chalcocite (combined reflected and transmitted light). The E and tennantite-enargite stage (TES) vein nomenclature was instigated in this study to designate the polymetallic epithermal veins. Abbreviations: alun = alunite, bn = bornite, cc = chalcocite, cp = chalcopyrite, dg = digenite, dias = diaspore, dj = djurleite, dk = dickite, en = enargite, mw = mawsonite, prl = pyrophyllite, py = pyrite, qtz = quartz, tn = tennantite, zun = zunyite.

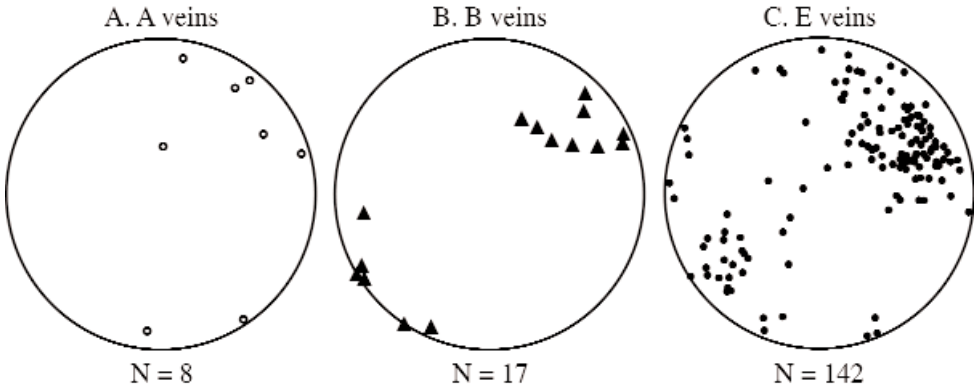


FIG. 13. Lower hemisphere equal area projections of mineralized veins. Data are separated into the main paragenetic stages. A. Early-stage chalcopyrite-bornite A veins. B. Quartz-molybdenite B veins. C. Late-stage polymetallic E veins. Data from Lee (1994). The lack of data for A veins prevents any meaningful conclusion of preferred orientation. By contrast, the orientation data for B and E veins are consistent with formation during normal movement in the Rosario fault system. Small fault offsets and microdeformation textures (e.g., milled sulfide microbreccias) that cut E veins support the interpretation that dextral strike-slip reactivation postdated deposition of high-sulfidation state sulfide assemblages.

on the physicochemical conditions of mineralization during most of the paragenetic stages at Rosario and La Grande (specifically, stages A, B, C, E, and TES).

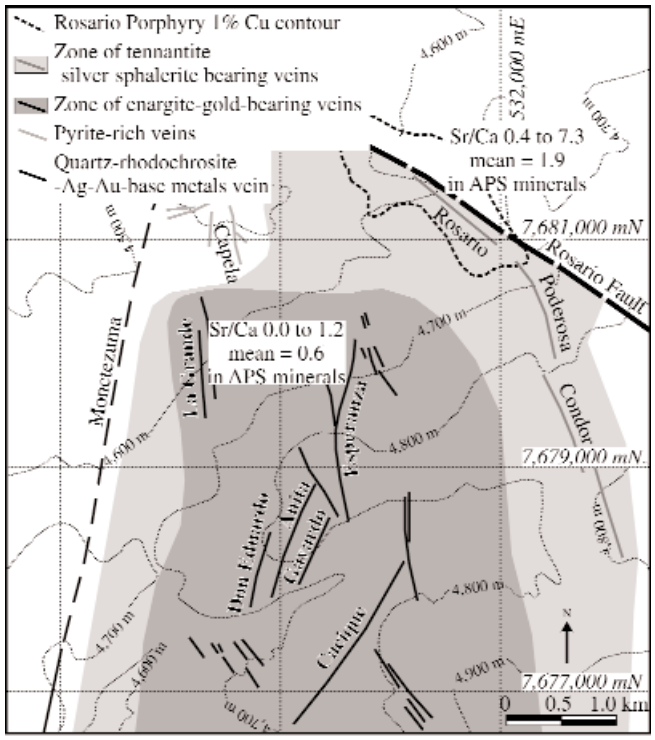


FIG. 14. Plan view of the major veins in the Rosario-Cerro La Grande area. Colored zones highlight the distribution of base and precious metals. Enargite-bearing veins with low Ag/Au occur at Cerro La Grande. Tennantite veins with high Ag/Au occur in the north and east at Rosario and/or Poderosa and Condor, respectively. Sr/Ca values of aluminum-phosphate-sulfate (APS) minerals (determined by electron microprobe analysis) in the advanced argillic altered rocks at Rosario and La Grande are also shown. The La Grande and Rosario veins are both exposed between 4,600 and 4,100 m a.s.l., with some of the Rosario veins open downdip below 4,100 m. Veins in Cerro La Grande crop out at 4,800 m a.s.l. The deepest exposures occur in the Don Eduardo and Forastera veins, which have been worked from surface to elevations of 4,610 and 4,530 m, respectively (190–350 m below surface).

Samples were selected for microthermometric analyses on the basis of Roedder's (1984) criteria, specifically the fluid inclusions trapped a single, homogeneous phase (as indicated by constant liquid/vapor ratios and coherent homogenization temperature and salinity data obtained from discrete fluid inclusion populations); and the inclusions represent an isochoric (constant volume) system, so that after trapping, nothing has been added to, or removed from, the inclusions (i.e., no petrographic evidence for mineral growth on the inclusion walls or for leakage or reequilibration of inclusions after entrapment, such as inclusions with scalloped walls, annular or hooklike morphologies, or a regular-shaped parent inclusion that is surrounded by a halo of small daughter fluid inclusions, e.g., Ayllon et al., 2003). We avoided samples with obvious macroscopic and/or petrographic evidence for postmineralization deformation, which could have caused reopening and reequilibration of the fluid inclusions.

Temperatures of liquid-vapor homogenization, dissolution of salt daughter crystals, and the final melting of ice were measured on a Linkam MDS600 heating/freezing stage. The Linkam stage has a maximum temperature limit of 600ºC and was calibrated using synthetic fluid inclusions supplied by Synflinc Inc., with precisions of ±1.0ºC for heating and 0.3ºC for freezing. Heating and freezing experiments were completed on 470 fluid inclusions.

Salinities of halite-undersaturated fluid inclusions, reported as weight percent NaCl equivalent (wt % NaCl equiv), were calculated from freezing point depression temperatures (final ice melting), using the method of Potter et al. (1978). Weight percent NaCl equivalent was calculated for halite-saturated fluid inclusions by the algorithm of Sterner et al. (1988). The computer program SALTY (Bodnar et al., 1989) was used to calculate the concentrations of NaCl and KCl in fluid inclusions that contained both halite and sylvite daughter crystals.

### *Populations*

The fluid inclusion types encountered in this study are summarized in Figure 15 and Table 2. Fluid inclusion sample numbers are listed in Table 3 and sample locations are shown in Figures 7 and 8. Three major types of fluid inclusions and

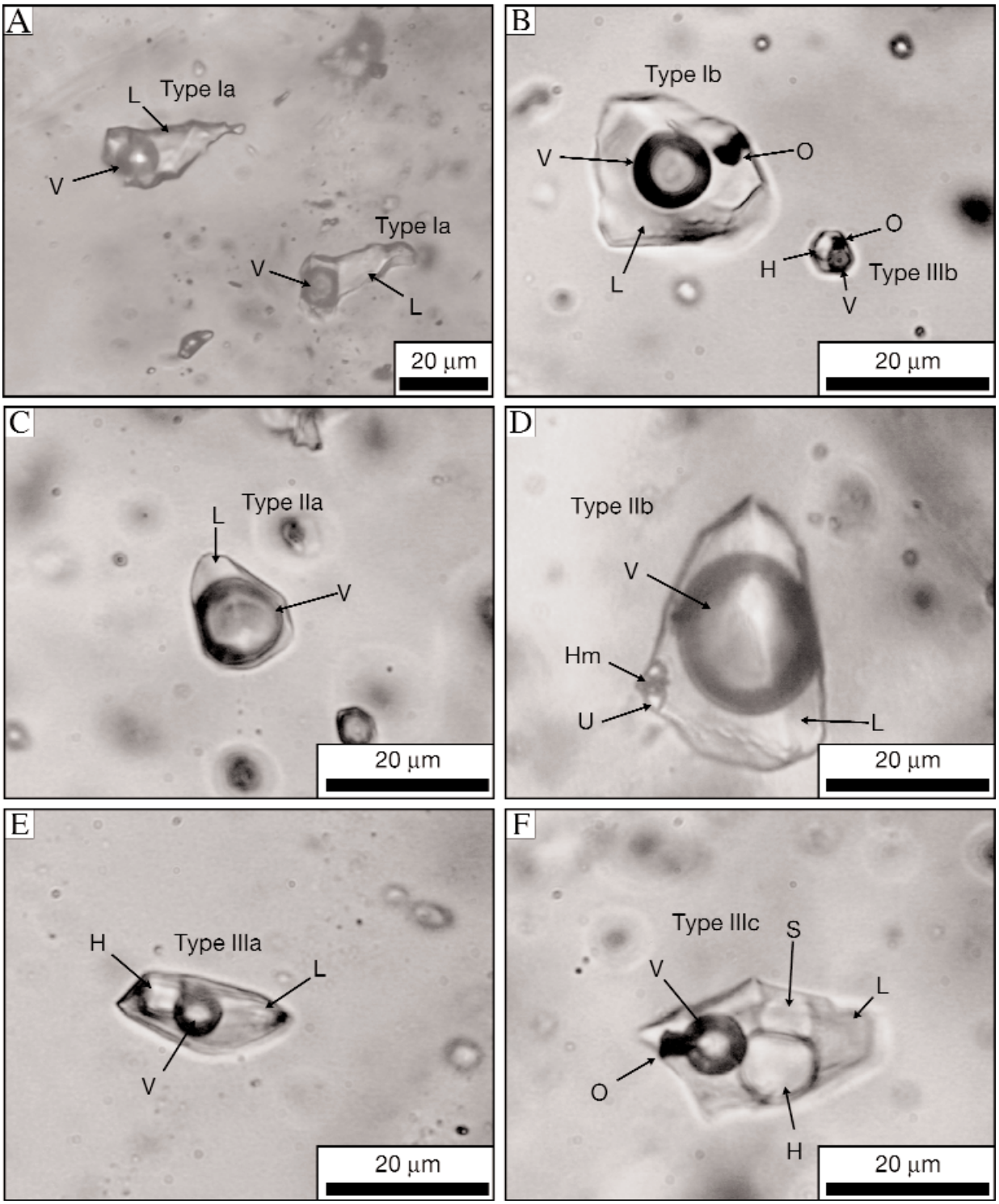


FIG. 15. Photomicrographs of fluid inclusions in vein quartz from Rosario (plane-polarized light. A. Liquid-rich Ia inclusions in quartz from an E vein. B. Liquid-rich Ib inclusion that contains a solid opaque mineral trapped next to type IIIb inclusions in an A-3 vein. The brine inclusion contains halite and an opaque mineral. C. Type IIa vapor-rich inclusion from an A-3 vein, showing characteristic negative crystal shape. D. Vapor-rich inclusion from an A-3 vein, typical of the IIb type with negative crystal shape and multiple daughter minerals. The solid orange-colored phase is hematite, the prismatic crystal is birefringent and may be anhydrite. The aqueous component of this inclusion homogenized by expansion of the bubble, even though it contains approximately 50 vol percent liquid. The presence of daughter minerals and substantial liquid suggests that liquid and gas may have been trapped heterogeneously in this inclusion. E. Type IIIa brine inclusion from an E vein containing a single cubic salt phase identified as halite. F. Brine inclusion from an A-3 vein characteristic of type IIIc. It contains multiple daughter crystals identified as halite, sylvite, and an opaque phase. Abbreviations: A = anisotropic daughter mineral, Cpy = chalcopyrite, H = halite, Hm = hematite, L = liquid, O = opaque, S = sylvite, V = vapor.

TABLE 2. Summary of Fluid Inclusion Types, Morphology, Phases Present at 25ºC, and Homogenization Behavior

| Fluid inclusions | | | Phases at 25ºC | | | | Homogenization behavior |
|---|---|---|---|---|---|---|---|
| Type | Subtype[1] | Inclusion shape | Size ($\mu$m) | Number | Dominant | Types | |
| I | A | Elongate, negative crystals or rounded, less commonly irregular | <5–50 | 2 | Liquid | Liquid + vapor | Vapor disappearance |
| | B | Elongate, negative crystals or rounded, less commonly irregular | <5–30 | 3-5 | Liquid | Liquid + vapor ± opaque ± hematite ± insoluble unknown | Vapor disappearance |
| II | A | Stubby negative crystals, less commonly rounded | 5–30 | 2 | Vapor | Vapor + liquid | Liquid disappearance |
| | B | Stubby negative crystals, less commonly rounded | 5–30 | 3–5 | Vapor | Vapor + liquid + opaque ± hematite ± insoluble unknowns | Liquid disappearance |
| III | $a_l$ | Negative crystals, rounded or irregular | 5–30 | 3 | Liquid | Liquid + vapor + halite | Vapor disappearance |
| | $a_h$ | Negative crystals, rounded or irregular | 5–30 | 3 | Liquid | Liquid + vapor + halite | Salt dissolution |
| | $b_l$ | Negative crystals, rounded or irregular | <5–40 | 4–6 | Liquid | Liquid + vapor + halite ± hematite ± insoluble unknown ± opaque | Vapor disappearance |
| | $b_h$ | Negative crystals, rounded or irregular | <5–40 | 4–6 | Liquid | Liquid + vapor + halite ± hematite ± insoluble unknown ± opaque | Salt dissolution |
| | $c_l$ | Negative crystals, rounded or irregular | 10–40 | 4–7 | Liquid | Liquid + vapor + halite + sylvite ± hematite ± insoluble unknown ± opaque | Vapor disappearance |
| | $c_h$ | Negative crystals, rounded or irregular | 10–40 | 4–7 | Liquid | Liquid + vapor + halite + sylvite ± hematite ± insoluble unknown ± opaque | Salt dissolution |
| IV | | Rounded or irregular | 20–40 | 3–11 | Daughter minerals | silicate daughter minerals + shrinkage bubble ± cubic mineral (halite?) ± opaque ± liquid | Did not homogenize below 600ºC |

[1] $_l$ indicates fluid inclusions that homogenize by disappearance of the vapor bubble, $_h$ indicates inclusions that homogenize by halite dissolution

10 subtypes have been identified at Rosario and La Grande. They have been classified by the number of phases present at room temperature, using the scheme of Nash (1976). Type I fluid inclusions are liquid rich, halite undersaturated, and homogenize by disappearance of the vapor phase (Fig. 15A-B). Type II fluid inclusions are vapor rich and homogenize by expansion of the vapor phase (Fig. 15C-D). Type II fluid inclusions less than 6 $\mu$m are generally filled entirely by vapor, whereas larger type II fluid inclusions usually contain a small amount of liquid. Type III fluid inclusions are halite saturated and homogenize either by disappearance of the vapor phase (Tv→l) or dissolution of the halite daughter crystal (Ts halite). Type III fluid inclusions may contain only a single soluble daughter mineral (e.g., halite; Fig. 15E) or may contain halite plus one or more insoluble daughter minerals. Some type III fluid inclusions contain halite and sylvite, as well as multiple insoluble daughter minerals (Fig. 15F).

All veins in the Rosario deposit have been repeatedly fractured in the presence of an aqueous fluid. This has resulted in complex overprinting of various fluid inclusion populations, so it is almost impossible to establish age relationships among the different fluid inclusion types within any single vein of quartz. It is not possible to distinguish conclusively between overprinting and simultaneous trapping of different fluids. For this reason, fluid inclusions have not been classified as primary, secondary, or pseudosecondary. Instead, we have adopted a method of relating groups of fluid inclusions to the various stages of vein development similar to that outlined by Bodnar and Beane (1980) and Bloom (1981). Fluid inclusion populations containing multiple inclusion types must satisfy the following criteria if they are considered to have coexisted at the time of trapping (e.g, type II and type III inclusions trapped during phase separation): (1) they occur in close proximity not separated by more than 5 to 50 $\mu$m, (2) they have overlapping temperatures of homogeniztion, and (3) they do not occur in younger vein stages.

Type I fluid inclusions are observed in every vein stage at Rosario and are also present in the E/TES (massive sulfide) veins at La Grande. The wide range of homogenization temperatures and salinities for the type I inclusions in any single quartz vein may reflect complex overprinting of different fluid types. We consider that the most reliable homogenization and salinity data for type I inclusions occur in the tennantite-enargite stage (TES) veins, as these were the last to form. Type I fluid inclusion microthermometric data from the other vein stages are treated with caution. Low-density type

TABLE 3. Summary of Fluid Inclusion Populations in Porphyry-Type Veins, Listed with the Corresponding Vein Stage and Alteration Assemblage in the Rosario Deposits

| Vein stage[1,2] | Vein mineralogy | Alteration assemblage | Inclusion types[3] | $T_h$[4] v→l min to max (°C) | Model[5] $T_h$[4] v→l (°C) | Ts[6] sylvite min to max (°C) | Model[5] Ts[4] sylvite (°C) | Ts[6] halite min to max (°C) | Model[5] Ts[4] halite (°C) | Salinity min to max (wt % NaCl equiv) | Salinity mean (wt % NaCl equiv) |
|---|---|---|---|---|---|---|---|---|---|---|---|
| Porphyry-type veins | | | | | | | | | | | |
| A-2 | Qtz-alb-bi-cp-py | Bi-alb | IIa + IIb | 385 to >600 | 493 to >600 | - | - | - | - | 1.8 to 18.9 | 10.8 |
| | | | $IIIa_h$ + $IIIb_h$ | 158 to 298 | 241 to 298 | - | - | 246 to 497 | 359 to 497 | 34.4 to 59.3 | 44.1 |
| | | | Ia + Ib | 320 to 524 | 426 to 524 | - | - | - | - | 13.0 to 25.2 | 17.7 |
| | | | $IIIa_l$ + $IIIb_l$ | 260 to 433 | 333 to 433 | - | - | 149 to 401 | 285 to 401 | 29.7 to 47.6 | 37.9 |
| A-3 | Qtz-K fsp-bn-cp | K-fsp | IIa + IIb | 369 to >600 | 500 to >600 | - | - | - | - | 3.3 to 21.4 | 12.3 |
| | | | $IIIa_h$ +$IIIb_h$ + $IIc_h$ | 124 to 449 | 256 to 449 | 52 to 374 | 103 to 374 | 215 to 593 | 354 to 593 | 33.0 to 73.0 | 45.3 |
| | | | $IIIa_l$ + $IIIb_l$ | 223 to 539 | 326 to 539 | 56 to 136 | 96 to 136 | 171 to 460 | 263 to 460 | 31.0 to 55.0 | 37.3 |
| | | | Ia + Ib | 203 to 451 | 317 to 451 | - | - | - | - | 1.2 to 25.6 | 14.5 |
| | | | IV | 336 to 490 | 425 to 490 | - | - | - | - | - | - |
| B | Qtz-K fsp-ill-mo | (K-fsp-ill) | Ia + Ib | 261 to 408 | 349 to 408 | - | - | - | - | 1.3 to 23 | 8.5 |
| | | | IIa | 342 to 457 | 407 to 457 | - | - | - | - | 2.7 to 7.7 | 5.2 |
| C | Qtz-cp-py-ill-chl | Ill-chl | Ia + Ib | 153 to 408 | 245 to 408 | - | - | - | - | 3.1 to 23 | 15.8 |
| Polymetallic veins | | | | | | | | | | | |
| E | Py-bn-cp-cc-qtz | Qtz-alun-dias | Ia + Ib | 153 to 453 | 353 to 453 | - | - | - | - | 1.7 to 23.0 | 12.8 |
| | | | IIa | 404 to 484 | 436 to 484 | - | - | - | - | 4.5 to 12.5 | 8.6 |
| | | | $IIIa_h$ + $IIIb_h$ | 189 to 246 | 213 to 246 | - | - | 242 to 310 | 278 to 310 | 34.2 to 38.9 | 36.7 |
| | | | $IIIa_l$ + $IIIb_l$ | 250 to 347 | 293 to 347 | | | 149 to 221 | 175 to 221 | 29.6 to 33.0 | 30.8 |
| Tennantite-enargite stage veins (TES) | | | | | | | | | | | |
| Rosario | Tn-en-qtz | Prl-dick | Ia + Ib | 195 to 364 | 269 to 364 | - | - | - | - | 0.7 to 22.2 | 6.1 |
| La Grande | En-qtz | Prl-dick | Ia + Ib | 236 to 342 | 297 to 342 | - | - | - | - | 0.7 to 6.8 | 3.5 |

- = no data

Mineral abbreviations: alb = albite, alun = alunite, bi = biotite, bn = bornite, cc = chalcocite, chl = chlorite, cp = chalcopyrite, dias = diaspore, dick = dickite, en = enargite, ill = illite, K fsp = K feldspar, mo = molybdenite, prl = pyrophyllite, py = pyrite, qtz = quartz, tn = tennantite

[1] Rosario fluid inclusion samples (see Fig. 7 for sample localities); A-2 veins: R990007 and R990124; A-3 veins: R990106 and R990108; B veins: R990108; C veins: R990085; E veins: R990170 and R200021; tennantite-enargite stage veins: R200021

[2] La Grande fluid inclusion samples (see Fig. 8 for sample locations); Tennantite-enargite stage veins: R990299 and R990324

[3] $_l$ indicates fluid inclusions that homogenize by disappearance of the vapor bubble, $_h$ indicates fluid inclusions that homogenize by halite dissolution

[4] $T_h$ = temperature of vapor bubble disappearance in type I and type III fluid inclusions or temperature of complete vapor bubble expansion in type II fluid inclusions

[5] Model temperature is taken as the range from the mean to maximum homogenization temperature for a fluid inclusion type in a given sample

[6] Ts = temperature of salt dissolution

II fluid inclusions are most abundant in A-2 and A-3 veins but small quantities also occur in B and E veins. In general, homogenization temperatures of type II inclusions in A-2 and A-3 veins are higher than those in B and E veins. We therefore infer that the vapor-rich fluids trapped in A-2 and A-3 veins were different from those trapped in the later B and E vein stages.

Type III saline and hypersaline brine fluid inclusions occur mainly in the A-2 and A-3 vein stages where they coexist with the type I and II fluid inclusions. The abundance of type II fluid inclusions in A-2 and A-3 veins exceeds, by an order of magnitude, that of type III fluid inclusions which homogenize by vapor disappearance. However, homogenization temperatures of the small number of vapor to liquid homogenizing type III fluid inclusions correlate well with homogenization temperatures of coexisting type II inclusions. We infer that overlapping homogenization temperatures indicate simultaneous trapping of two different fluids. Fluid inclusion populations from each vein stage are summarized in Table 3. Microthermometric data from each vein stage is presented in Figures 16 and 17.

*Fluid inclusions in A veins:* Fluid inclusions in A-2 veins homogenize between 246º and >600ºC (Figs. 16A-B, 17A), with 65 percent of all fluid inclusions homogenizing at temperatures >400ºC (Table 3). Type IIa and IIb vapor-dominated fluid inclusions have the highest apparent homogenization temperatures (385º to >600ºC), although these may be 150° to 300ºC below the actual homogenization temperatures owing to difficulty observing the final disappearance of the liquid (Bodnar et al., 1985). The salinities of vapor-rich fluid inclusions ranged from 1.8 to 18.9 wt percent NaCl equiv (Figs. 16C, 17A).

More than half of the type III hypersaline fluid inclusions homogenized by halite dissolution, with the remaining 40 percent homogenizing by vapor disappearance. Final homogenization temperatures, either by vapor disappearance or halite dissolution, ranged from 255º to 497ºC and averaged 350ºC (Figs. 16B, 17A, Table 3). Salt dissolution temperatures for type III fluid inclusions ranged between 246º to 497ºC, corresponding with calculated salinities of 34.4 to 59.3 wt percent NaCl equiv (avg of 41.7 wt % NaCl equiv; Figs. 16C, 17A). Liquid-rich type I fluid inclusions have a salinity range of 13 to 25.2 wt percent NaCl equiv and homogenize from 320º to 524ºC (avg of 426ºC).

A-3 veins contain abundant type II vapor-rich fluid inclusions that homogenize between 369º to >600ºC (Table 3). Salinities of the type II fluid inclusions vary from 3.3 to 21.4 wt percent NaCl equiv (Figs. 16C, 17A). These temperatures correlate with data from a small number of type III inclusions that homogenize by vapor disappearance between 447º and 539ºC (Figs. 16A, 17A). Over three-quarters of the type III hypersaline fluid inclusions analyzed from A-3 veins homogenized by halite dissolution with a bimodal distribution of 215º to 300º and 340º to 480ºC. Salinities calculated from these halite dissolution temperatures range between 33 and 73 wt percent NaCl equiv (mean = 45.3 wt % NaCl equiv; Fig. 16C). Some type IIIc liquid + vapor + halite inclusions are present, with KCl concentrations that range from 12.7 to 19 wt percent. The total salinities of type IIIc fluid inclusions range from 43.4 to 72.8 wt percent NaCl + KCl equiv. Liquid-rich type Ia and Ib fluid inclusions occur in the same quartz grains as vapor-rich (type II) and hypersaline brine (type III) inclusions and show variable homogenization temperatures and salinities that range from 203º to 451ºC and 1.2 to 25.6 wt percent NaCl equiv, respectively (Table 3, Figs. 16B-C, 17A).

*Fluid inclusions in B veins:* B veins are characterized by type I and II inclusions, which homogenize between 261º and 457ºC (Table 3, Figs. 16D-E, 17B), with 60 percent of fluid inclusions homogenizing at temperatures >350ºC. The highest temperature of homogenization of liquid-rich fluid inclusions (>340ºC) overlaps the homogenization temperatures of coexisting vapor-rich fluid inclusions, which vary from 342º to 457ºC. Salinities of the type I and II fluid inclusions range from 1.3 to 23 and 2.7 to 7.7 wt percent NaCl equiv, respectively (Figs.16F, 17B).

*Fluid inclusions in C veins:* Type I fluid inclusions in C veins homogenize between 153º and 400ºC, although 90 percent of the data are between 200º and 300ºC (Table 3, Figs. 16G-H, 17C). Salinities range from 3.1 to 23 wt percent NaCl equiv (avg salinity = 15.8 wt % NaCl equiv, Figs. 16I, 17C), with 63 percent of analyses falling between the mean and maximum values (15.8–23 wt % NaCl equiv).

*Fluid inclusions in E veins:* Fluid inclusions in quartz gangue associated with pyrite-bornite-chalcopyrite massive sulfide veins (E veins) homogenize between 153º and 453ºC, with two discrete populations occurring between 200º to 320ºC (mode 300ºC) and 360º to 440ºC (mode 400ºC: Figs. 16J-K, 17D). Salinities of type I and II fluid inclusions vary from 1.7 to 23.0 wt percent NaCl equiv and have a mean of 12.8 wt percent NaCl equiv (Figs. 16L, 17D). The small number of type III fluid inclusions homogenize predominantly by halite dissolution between 149º and 314ºC, indicating salinities of 29.6 to 39.3 wt percent NaCl equiv. The high temperatures of homogenization (360º–440ºC) of type I fluid inclusions overlap with homogenization temperatures of the type II fluid inclusions (400º–500ºC), whereas the lower temperature population (200º–340ºC) corresponds with those of liquid-rich fluid inclusions measured in the TES veins.

*Fluid inclusions in tennantite-enargite (TES) veins:* Type I liquid-rich fluid inclusions in quartz associated with tennantite-enargite mineralization at Rosario homogenize between 155º and 364ºC. About 85 percent of these fluid inclusions homogenize between 220º and 320ºC (270ºC mean homogenization temperature: Figs. 16M-N, 17E). Calculated salinities are between 0.7 and 22.2, with an average of 6.1 wt percent NaCl equiv (Figs. 16O, 17E). At La Grande, inclusions in tennantite-enargite stage quartz sampled from 3,880-m elevation, have average temperatures of homogenization of 320ºC (±20°C). By contrast, quartz-hosted fluid inclusions from 4,280-m elevation have a mean homogenization temperature of 280ºC (±30°C). Calculated salinities range from 0.7 to 6.8 wt NaCl equiv for both samples.

### *Interpretation of microthermometry and pressure estimates*

In A-2 and A-3 veins, a small number of type III inclusions homogenize by disappearance of the vapor bubble at temperatures similar to that of coexisting low-density vapor-rich (type II) fluid inclusions (Fig. 16B), suggesting that brines and gases were present as separate phases (fluid immiscibility) when

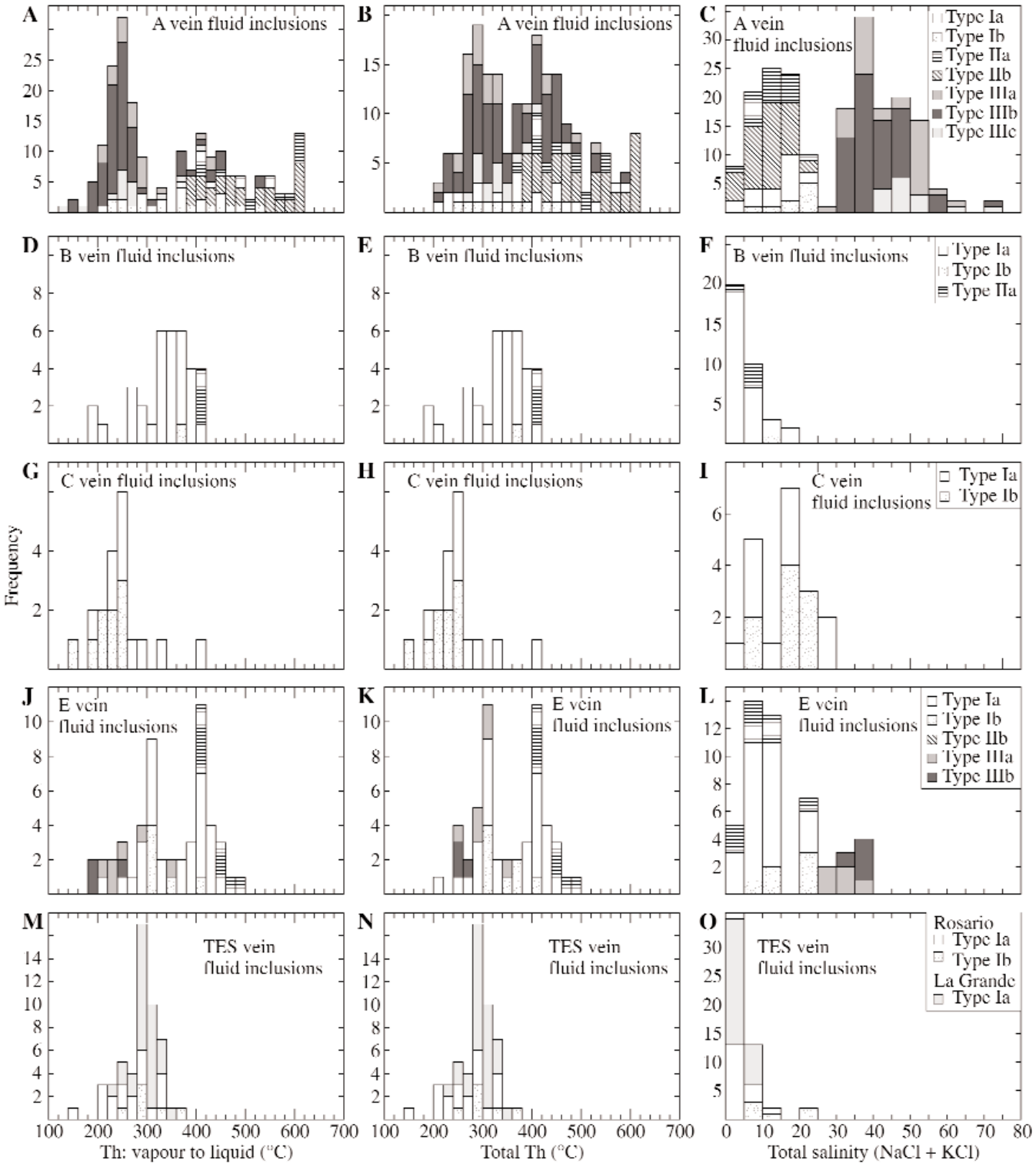


FIG. 16. Summary of microthermometric data for the various fluid inclusion populations. They are grouped across the page by population type and ordered down the page from the earliest formed fluid inclusions (A veins) to those formed last (TES veins). Histograms down the left-hand column summarize vapor-to-liquid homogenization temperatures for type I and type III inclusions. Homogenization temperatures of type II inclusions are the temperatures of homogenization to the vapor phase. The center column shows total homogenization temperature by either vapor to liquid, liquid to vapor, or by halite dissolution, whichever occurred last. The right-hand column depicts the salinities of all fluid inclusions, calculated either by final ice-melting temperature (e.g., for the liquid- and vapor-rich inclusions) or by halite dissolution temperature (e.g., for the brine inclusions). (A)-(C). Populations A-2 and A-3. (D)-(F). Population B. (G)-(I). Population C. (J)-(L). Population E. (M)-(O). Population TES.

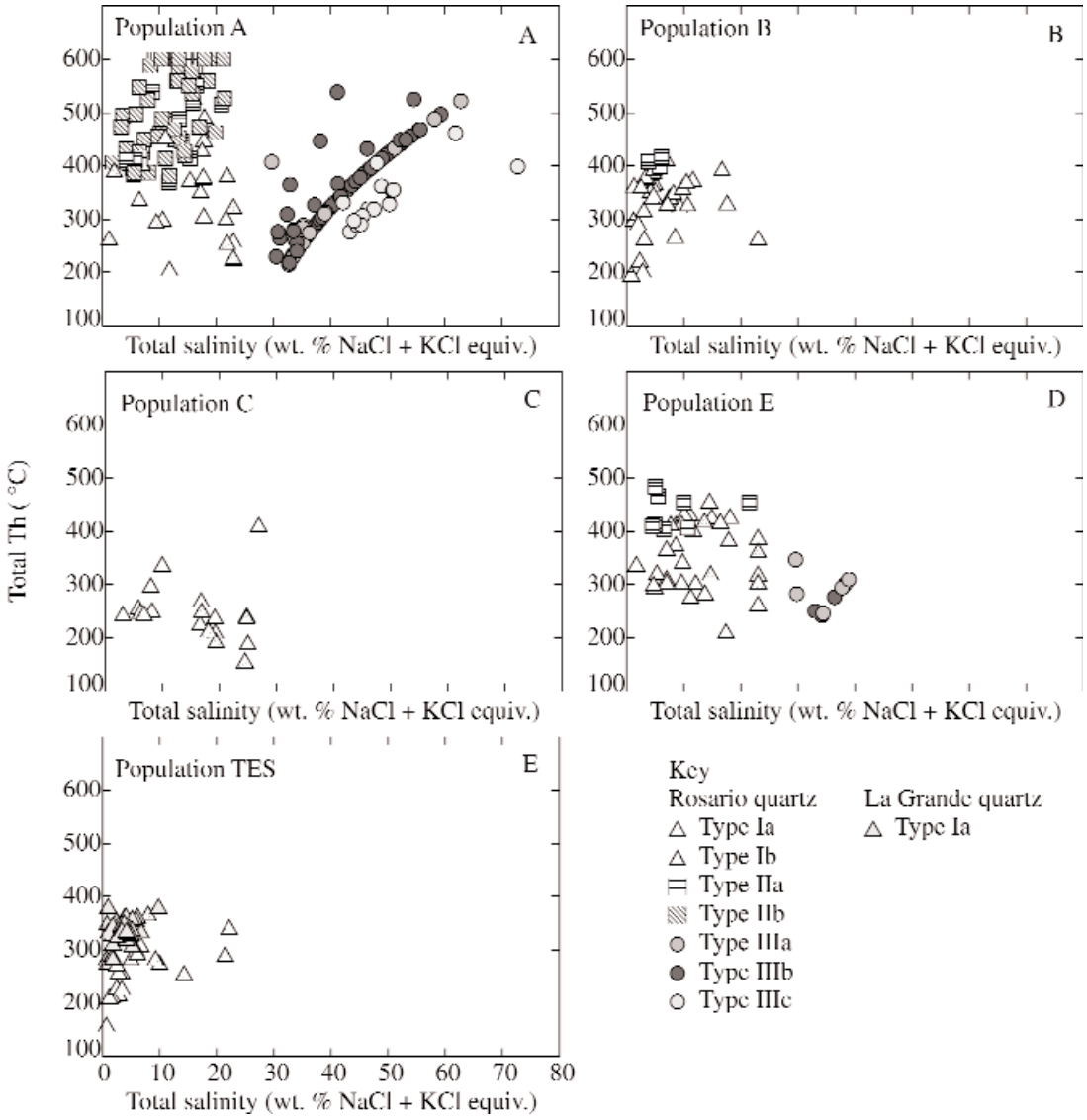


FIG. 17. Binary plots of total homogenization temperature vs. salinity for inclusions in each of the populations. A. A-2 and A-3 veins. B. B veins. C. C veins. D. E veins. E. Tennantite-enargite stage veins. Although the measured temperature ranges are large, average homogenization temperatures decrease from the A-2 and A-3 to the B and C veins. High-temperature type I and II fluid inclusions from quartz in E veins perturb the temporal cooling trend. These liquid- and vapor-rich inclusions typically occur in quartz associated with alunite, pyrite, and diaspore. A second population of low-temperature type I and III fluid inclusions are associated with quartz in the sulfide-rich parts of the E veins. Homogenization temperatures of the low-temperature type I inclusions in the overlap those in the tennantite-enargite stage (TES) veins. We interpret this relationship to indicate overprinting of E vein quartz by late TES fluids.

these fluids were trapped. Fluid inclusions that homogenize by halite dissolution exhibit a wide range of homogenization temperatures and salinities and constitute ~75 percent of type III fluid inclusions in A-2 and A-3 veins.

Halite-homogenizing fluid cannot be trapped in equilibrium with a vapor phase in the $H_2O$-NaCl system (Fig. 18; Roedder and Bodnar, 1980; Bodnar, 1994). The lack of solid halite inclusions or their relict shapes in A vein quartz suggest that accidental trapping of halite crystals was unlikely (e.g., Eastoe, 1982; Richards and Kerrich, 1993) and there is no evidence of postentrapment modification (e.g., Eastoe, 1978; Audetát and Günther, 1999). The highest temperature halite homogenizing fluid inclusions from Rosario (530ºC and 45 wt % NaCl equiv) potentially cooled isobarically from immiscible brine and vapor (Fig. 18, path A-A'). The minimum temperature of 200ºC for fluid inclusions that homogenize by halite dissolution at 390ºC corresponds with pressures as high as 2 kbars. However it is inferred that these elevated pressures possibly record fluid overpressuring caused by the tensile strength of the overlying rock rather than deep formation of the veins (e.g., Kontak and Clark, 2002). The data suggest that cooling and overpressuring may have existed down to 250ºC and salinities of ~35 wt percent NaCl (Fig. 18).

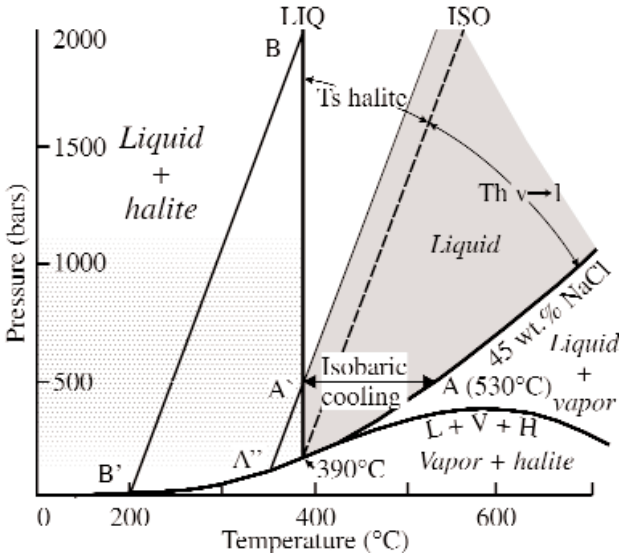


FIG. 18. Pressure-temperature diagram illustrating trapping conditions in the NaCl-$H_2O$ system, from 100° to 700°C for a 45 wt percent fluid, based on data of Bodnar (1994), Cline and Bodnar (1994), and Cline and Vanko (1995). The liquid-to-vapor curve (L-V) separates the stability field for liquid + vapor and liquid; the liquid-vapor-halite curve (L-V-H) separates stability fields for liquid + vapor and vapor + halite; the liquidus (LIQ) separates stability fields for liquid + halite and liquid. An isochore (ISO) divides the liquid-stable field into two regions; inclusions trapped on the high-temperature side of the isochore (Th v→l) will exhibit final homogenization to the liquid, whereas inclusions trapped on the low-temperature side of the isochore (Ts halite) will exhibit final homogenization via halite dissolution. Fluids that undergo final homogenization by halite dissolution are interpreted to have formed by isobaric cooling. The example illustrated here is a 45 wt percent NaCl fluid that evolved by phase separation on the liquid-vapor curve (L-V) at ca. 530°C (path A-A'). Inclusions trapped in the gray shaded region homogenized to the liquid between 200° and 350°C (between paths A'-A" and B-B') and exhibited final homogenization at ca. 390°C (between A' and B). Those inclusions that homogenized to liquid at temperatures down to 200°C were trapped at pressures as high as 2 kbars, implying that the cooling fluids were overpressured. The interpretation that fluid pressures fluctuated during vein formation at Rosario is based on the multiple crosscutting relationships and crack-seal textures in the A-3 veins. (e.g., Fig. 11D).

Trapping pressures can be determined from the behavior of immiscible vapor-rich and brine fluid inclusions in the NaCl-$H_2O$ system (Bodnar et al., 1985; Fournier, 1999). The minimum pressure of 500 bars is estimated for trapping of high-temperature type III fluid inclusions that homogenize by vapor bubble disappearance in the A-3 veins (Fig. 18). At this pressure and at 450° to 540°C, the rock should be almost ductile and can behave in a plastic manner, preventing formation of open fractures, except for episodic shear failure (Fournier, 1991, 1999). If pressures were lithostatic this would have required an overburden of at least 2 km. The "wormy," discontinuous and segmented morphologies of the earliest vein stages at Rosario (M and A veins) are consistent with this interpretation.

Coexisting high-temperature vapor and liquid-rich fluid inclusions in B veins implies that the fluids were boiling. At a salinity of 10 wt percent NaCl equiv, boiling of a 350°C fluid corresponds to a minimum pressure of 200 bars. At this temperature, the rock behaves in a brittle fashion, indicating that the pressure regime was hydrostatic. This estimate is consistent with the B veins having formed at a similar depth as A veins (~2 km; Haas, 1971) but under hydrostatic pressure. Temperatures of 250° to 350°C and depths of at least 1.8 km are indicated for the formation of C veins, as there is no evidence of boiling.

Type I and II fluid inclusions in quartz from E veins homogenize at about 330° to 450°C. In Figure 19, the range of temperatures is plotted in histograms as a function of depth below the paleosurface compared to the hydrostatic and lithostatic boiling curves. The range of homogenization temperatures possibly reflects discrete fluid compositions, differences in elevation of the paleowater table, or changes from lithostatic to hydrostatic pressures during formation of E veins. The presence of brine inclusions that homogenize by halite dissolution in the same vein quartz are consistent with high confining pressures. Thus, E veins may have formed as the pressure fluctuated between lithostatic and hydrostatic conditions. Fluid overpressuring also could have occurred in veins sealed by sulfide and quartz deposition. Boiling of a 10 wt percent NaCl fluid in the E veins at these temperatures corresponds to a minimum pressure of 200 bars, similar to the A and B veins. Under lithostatic conditions, the minimum formation depth is estimated to be 0.8 km, but if the boiling fluids contained $CO_2$ and other volatiles, then the depth would have been greater (Hedenquist and Henley, 1985).

Veins of the tennantite-enargite stage formed at depths of greater than 600 m because there is no evidence of phase separation in inclusions that homogenized at 270°C. In the La Grande vein, the tennantite-enargite stage veins formed from

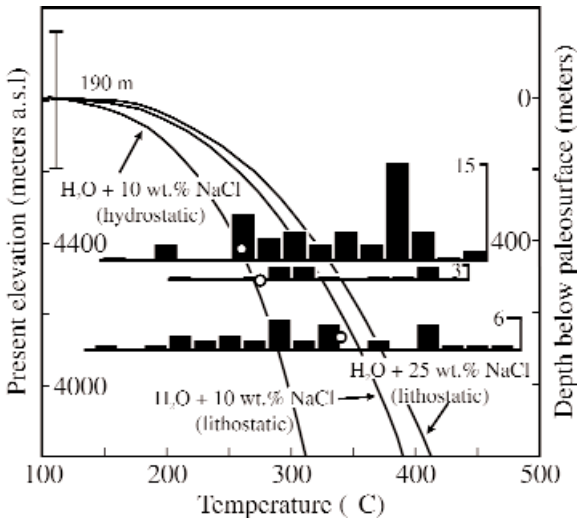


FIG. 19. Fluid inclusion temperatures from three E vein samples plotted in histograms as a function of depth compared to hydrostatic (10 wt % NaCl) and lithostatic (10 and 25 wt % NaCl) vapor-saturated curves. Also shown are the temperatures calculated, based on $\Delta^{34}S_{SO_4-FeS_2}$, for three coexisting alunite-pyrite samples (white-filled circles; Masterman, 2003). The hydrostatic boiling curve was calculated using the data of Haas (1971) and fitted to the low-temperature alunite-pyrite equilibrium pairs. The corresponding lithostatic boiling curves were plotted relative to the hydrostatic curve using the data of Fournier (1987). Inclusions that homogenize to the right of the lithostatic boiling curves were possibly trapped when fluids were overpressured. Alternatively, these inclusions may have been trapped in veins that formed deep in the system, then reopened at shallow depth in the presence of a different hydrothermal fluid. An uncertainty of ±190 m, based on the estimated uncertainty of alunite-pyrite temperatures, is shown for the hydrostatic boiling curve at a temperature of 275°C.

nonboiling fluids at a minimum depth of 720 to 1,160 m beneath the water table (280º–310ºC and ~3 wt % NaCl equiv).

*Rate of exhumation*

The paleosurface at Rosario was at least 1,200 to 1,300 m above the present surface during formation of the A and B veins based on minimum estimates of pressure and depth. It was eroded to approximately 1,000 m above the present surface by the time the C veins had formed and was at least 400 m above the present surface during formation of the E veins. Assuming the paleowater table was near surface when the tennantite-enargite veins formed, then the paleosurface was at least 200 m above the present surface at Rosario and 200 to 300 m above that at Cerro La Grande.

The cooling age of alunite (32.6 ± 0.3 Ma), associated with the formation of the E veins, is about 1.8 m.y. younger than that of primary biotite and illite (34.4 ± 0.3 and 34.1 ± 0.6 Ma, respectively: Masterman et al., 2004), which reflects the ages of the A and B veins at Rosario. However, the age of alunite is indistinguishable from that of hydrothermal muscovite (32.9 ± 0.6 Ma: Clark et al., 1998), implying that formation of E veins and the tennantite-enargite stage was broadly contemporaneous or that the Ar systematics of alunite were reset during muscovite formation. Based on the temporally constrained pressure-depth estimates, a minimum of 1 km of overburden is estimated to have been eroded at Rosario over a 1.8-m.y. period, which equates to an exhumation rate of 600 m/m.y. This rate is almost twice the rate of exhumation estimated by Maksaev and Zentilli (2000) based on fission track data from the Domeyko Cordillera. The exhumation rate at Rosario has been ~10 m/m.y. since the formation of the E and TES veins. This is less than the average rate (50 m/m.y.) estimated for the corresponding period across the Domeyko Cordillera by Maksaev and Zentilli (2000).

## Discussion and Conclusions

The conclusions drawn in the following sections are based on a limited fluid inclusion database and could change if more data were collected. Furthermore, the range of temperatures of homogenization and ice melting in the different fluid inclusions does not permit a rigorous analysis of the fluid evolution in the vein system at Rosario. However, a plausible model can be constructed from a consideration of the phase relationships in the NaCl-$H_2O$ system, as described by Bodnar et al. (1985) and Hedenquist et al. (1998; Fig. 20). The interpretation of fluid evolution in Figure 20 is only one possible scenario guided by average trapping temperatures and salinities observed in the fluid inclusions. Temporal evolution of the Rosario porphyry copper deposit is illustrated in Figure 21.

*Rosario stock emplacement and early K silicate alteration*

Primary biotite in the Rosario Porphyry cooled through its closure temperature at 34.4 Ma (Masterman et al., 2004), indicating that the stock intruded the Permian volcanic terrane some time before this. Based on the crosscutting relationships between M, A-1, A-2, and A-3 veins, it is possible that the magnetite alteration assemblage and some of the biotite-albite alteration assemblage formed prior to emplacement of the Rosario Porphyry.

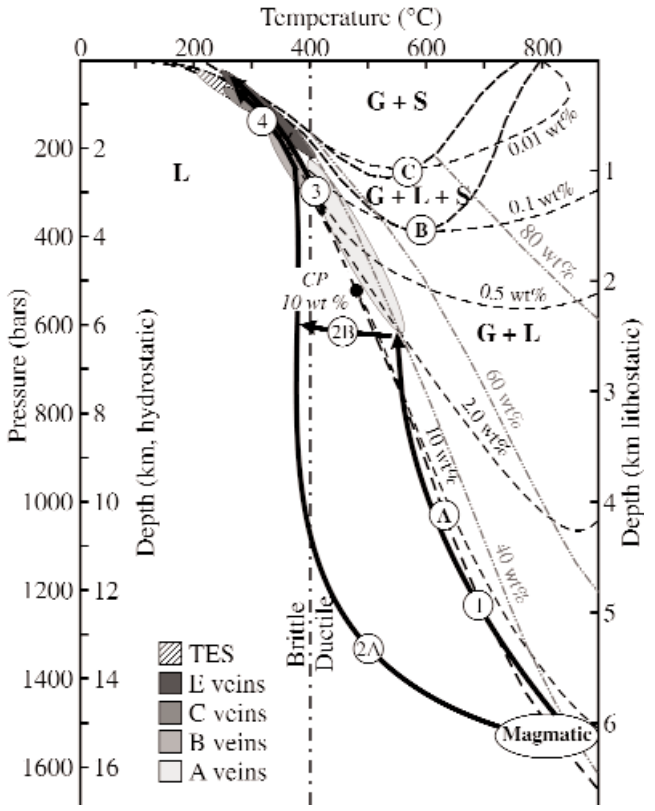


FIG. 20. Pressure-temperature diagram showing phase relationships in the NaCl-$H_2O$ system at lithostatic and hydrostatic pressures. Based on data of Bodnar et al. (1985) and Pitzer and Pabalan (1986), adapted from Fournier (1987, 1999) and Muntean and Einaudi (2001). G = gas, L = liquid, S = solid salt. Double dot-dashed lines are contours of constant wt percent NaCl dissolved in brine; short dashed lines are curves of the condensation points of steam containing the indicated wt percent NaCl. Curve A shows the boiling point curve for a 10 wt percent NaCl solution at pressures and temperatures below its critical point (CP) and the condensation curve for steam containing 10 wt percent NaCl at temperatures and pressures above the critical point. Curve B shows the three-phase boundary, G + L +S, for the system NaCl-$H_2O$; curve C shows the three-phase boundary, G + L + S, for the system NaCl-KCl-$H_2O$ with Na/K in solution fixed by equilibration with albite and K-feldspar at the indicated temperatures. The vertical dashed-dot line shows the approximate temperature of the brittle-ductile boundary for a strain rate of $10^{-14}$ $s^{-1}$ (Fournier, 1999). Ascent paths for the various exsolved magmatic fluids are shown with the corresponding fields of fluid inclusion populations.

At the site of formation of the A veins, magmatic-hydrothermal fluids had temperatures of 500ºC and consisted of hypersaline brine (~45 wt % NaCl) and low-density vapor (2 wt % NaCl). Fluid overpressuring and decompression cycling can account for the presence of brine inclusions that homogenize by halite dissolution in quartz samples from A-2 and A-3 veins. These veins also contain brine inclusions that homogenize by disappearance of the vapor bubble, which probably formed by phase separation when the rock fractured. A supercritical fluid containing about 10 wt percent NaCl at temperatures >600ºC is inferred to have exsolved from a crystallizing magma chamber at depths of 5 to 6 km. This fluid ascended in the single-phase field below its condensation curve and intersected its solvus at about 2.4 km (path 1, Fig. 20). In the two-phase region, the fluid separated into high-density brine and low-density vapor. Biotite-albite and K-feldspar

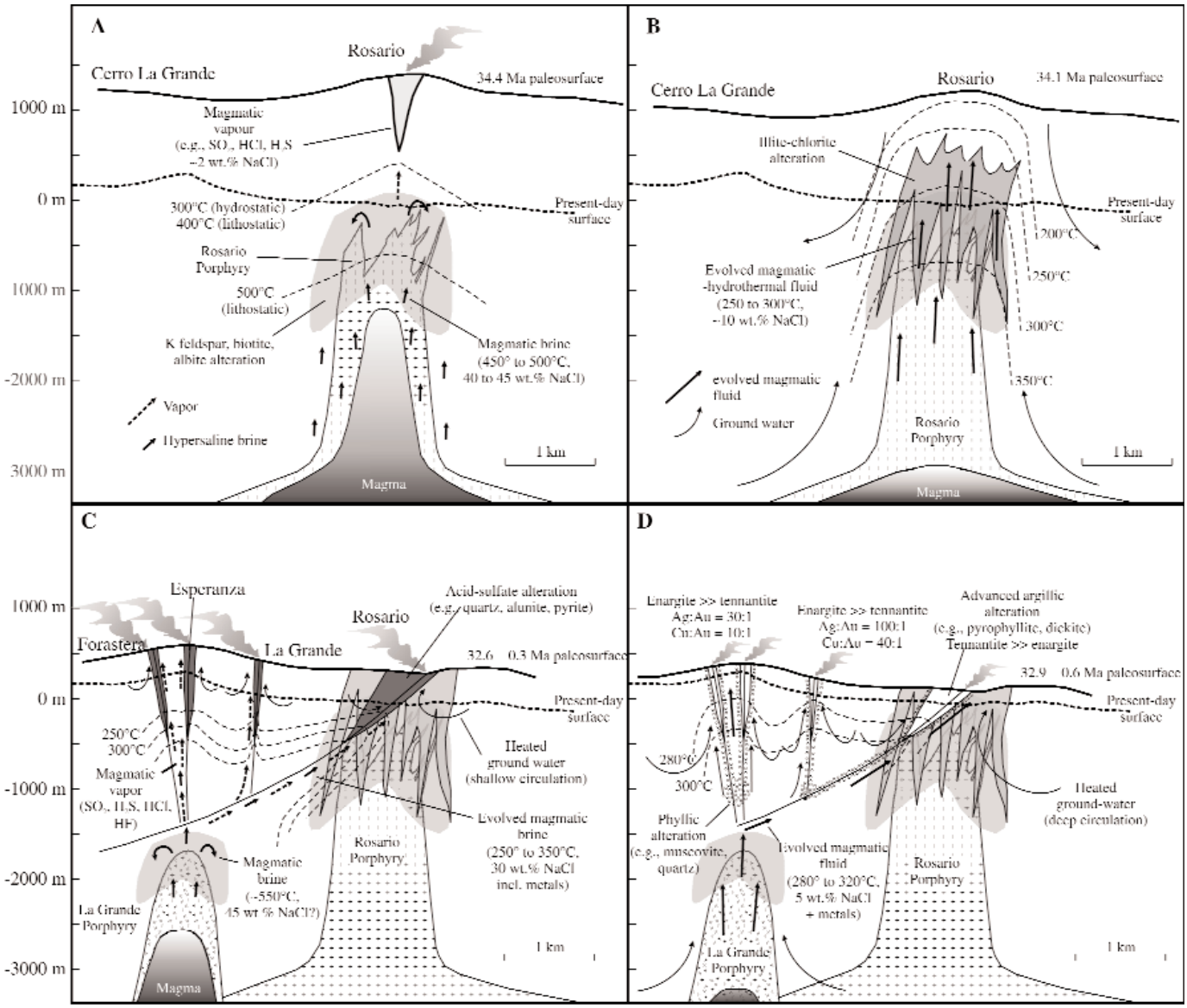


FIG. 21. Schematic cross sections through the Rosario and La Grande deposits, showing a model of the evolution of the Rosario magmatic-hydrothermal system. The present-day surface elevation at Rosario (4,600 m a.s.l.) is shown as zero meters relative to depth. A. Position of the paleosurface at ca. 34.4 Ma, relative to the present-day surface, at the time of A vein formation and related biotite-albite and K feldspar alteration. Location of the isotherms is based on fluid inclusion homogenization temperatures. Age constraints are from $^{40}Ar/^{39}Ar$ ages of igneous biotite and hydrothermal muscovite and alunite (Masterman et al., 2004). B. By about 34.0 Ma (min $^{40}Ar/^{39}Ar$ age of illite), the system was dominated by moderate-salinity, evolved magmatic-hydrothermal waters that produced the B and C veins. C. At 32.6 Ma, normal movement in the Rosario fault (shallow apparent dip) coincided with emplacement of a second intrusion beneath Cerro La Grande. Magmatic vapor ascended along the faults and condensed to form the quartz-alunite-pyrite-diaspore assemblage associated with E veins. Fault-valve activity in the veins promoted discharge of overpressured brines and subsequent self-sealing by sulfide deposition, consistent with sulfide breccia and cementation textures in the veins. D. Late-stage tennantite-enargite stage veins and related pyrophyllite-dickite and muscovite-quartz alteration formed by 32.3 Ma (min $^{39}Ar/^{40}Ar$ age of muscovite). The hydrothermal system was probably dominated by cool, low-salinity magmatic water mixed with a small amount of meteoric water. Tennantite, enargite, and precious metals were deposited during formation of pyrophyllite (and muscovite), presumably in response to mixing of the magmatic fluid with ground water.

alteration associated with A veins formed when the magmatic-hydrothermal brines interacted with the wall rocks (Fig. 21A).

*Collapse of the Rosario magmatic-hydrothermal system*

The highest concentrations of molybdenite occur in quartz veins within the Rosario Porphyry. These veins lack alteration envelopes, implying that the fluids were in equilibrium with the preexisting K-feldspar-biotite-albite alteration. Fluid inclusion microthermometry suggests that molybdenite was deposited with the quartz at temperatures between 350º and 400ºC. These fluids were cooler than those that caused the K-feldspar-biotite-albite alteration

(~500ºC). Thus molybdenite-bearing veins most likely formed as the Rosario Porphyry cooled and crystallized (Fig. 21B).

The illite-chlorite alteration assemblage at Rosario possibly reflects a domain of early acid neutralization by feldspar altered wall rocks (e.g., Heinrich, 2003, Fig. 21B). Fluid inclusion evidence indicates that the type C veins associated with illite-chlorite alteration formed at about 250ºC, consistent with mineral stability temperatures defined empirically for this assemblage by Reyes (1990). There are two possible pressure-temperature pathways for the type C hydrothermal fluids, assuming that they were of magmatic origin. The exsolved fluid either failed to intersect its solvus during ascent (path 2A, Fig. 20) and its salinity (15 wt % NaCl) reflects the bulk salinity of the magmatic fluid (Hedenquist et al., 1998), or the fluid was a low-density, moderate-salinity vapor that cooled and condensed isobarically (path 2B, Fig. 20; Heinrich, 2003). Both paths can potentially lead to sericite alteration by cooling, if the fluid was originally in equilibrium with K-feldspar and K/H mole ratios remain constant (Hemley, 1959; Sverjensky et al., 1991; Hedenquist et al., 1998).

Fluid inclusion data indicate that the fluids that formed the B veins had a temperature between 350º and 400ºC with an average salinity of 9 wt percent NaCl, whereas those that deposited the illite-chlorite assemblage reached a maximum temperature of 350ºC with an average salinity of 15 wt percent NaCl. At hydrostatic pressure, these temperatures are consistent with paleowater table depths of about 2 km, similar to the lithostatic depth inferred for the K silicate alteration. Thus there was little erosion between formation of K silicate and intermediate argillic alteration assemblages.

*Quartz-alunite-pyrite alteration and formation of the E veins*

At Rosario E veins were localized by the moderately southwest dipping Rosario fault, whereas at Cerro La Grande they are controlled by steep north-northeast trending faults (Fig. 21C). These structures are inferred to intersect ~1.6 km below the present surface at Cerro La Grande (Fig. 21C), implying that the acid fluids that caused the quartz-alunite-pyrite-diaspore alteration originated in the region beneath Cerro La Grande. Fluid inclusion data indicate that temperatures at the base of the quartz-alunite-pyrite zone were between 350º and 400ºC (4,140-m elevation), whereas temperatures decreased to 260ºC by the time the fluids ascended to 4,290-m elevation. The sharp temperature gradient implies that the hydrothermal system operated in the transition from lithostatic to hydrostatic pressures at about 800-m paleodepth. The fluid that formed quartz-alunite-pyrite-diaspore alteration associated with E veins may have followed path 3 in Figure 20, where a low-density vapor separated from the magmatic-hydrothermal fluid when it entered the two-phase (liquid + gas) region and ascended buoyantly ahead of the dense brine.

The hydrothermal system associated with the Rosario Porphyry had waned before the formation of the E veins at Rosario. Therefore, apparently increasing fluid temperatures in the late-stage veins (Figs. 16J-K, 17D) imply the presence of a blind intrusion located beneath or at the intersection of structures that controlled hydrothermal fluid flow at Cerro La Grande and Rosario (Fig. 21C). Fluid inclusion data from quartz gangue in E veins indicate that the fluids that deposited Cu-Fe sulfides had a moderate temperature (mean 290ºC) and salinity (30 wt % NaCl equiv). Some brine inclusions homogenized via halite dissolution, indicating that they possibly formed when the fluids were overpressured.

The Rosario fault system is a major northwest-trending suture in the Permo-Triassic basement block. It is parallel to the trans-arc lineaments of Richards (2000) but has a shallow dip and a normal sense of displacement. High-angle normal faults (~60º) are well oriented for reactivation but do not sustain significant fluid overpressures. In contrast, low-angle normal faults (~40º) tend not to be seismically active and may become locked (Jackson and White, 1989), thus promoting fluid overpressure (Sibson, 2001). Rupturing is inferred to have discharged overpressured fluids along the Rosario fault system, followed by self-sealing by sulfide deposition (e.g., Sibson, 2001). Breccia textures in the sulfide-rich parts of E veins are consistent with the possibility of cyclic fluid overpressuring and decompression during formation of the E veins. Similar processes most likely occurred during sinistral strike-slip movement in the La Grande fault system.

*Tennantite-enargite stage veins and pyrophyllite-dickite alteration*

Pyrophyllite and dickite alteration was synchronous with tennantite and enargite deposition at Rosario and La Grande, and Ag-rich tennantite (TES) veins at Rosario formed on the margins of the 32.9 Ma hydrothermal system. Proximal Au-rich enargite veins at Cerro La Grande occur directly above an inferred blind intrusion emplaced at this time. Fluid inclusion data indicate that quartz gangue in the TES veins was deposited at a minimum paleodepth of 600 m. The paleosurface was therefore at least 200 m above the present surface at Rosario if the paleowater table was near surface during formation of the tennantite-enargite stage veins. By contrast, the paleosurface was at least 1,200 m above the present surface during formation of the A and B veins, thus the Rosario porphyry system was therefore partially exhumed at the time the Rosario veins formed. Rapid exhumation at Rosario in the late Eocene-early Oligocene appears to have caused superposition of two distinct mineralization styles within the same ore deposit.

*Mechanism for rapid uplift*

Late Eocene exhumation rates in the Domeyko Cordillera (200–300 m/m.y.) reflect uplift and erosion caused by crustal thickening during the Incaic orogeny (Maksaev and Zentilli, 2000). However, these rates of exhumation are significantly lower than those required to superimpose high-sulfidation state massive sulfide veins onto the core of the Rosario porphyry. A mechanism that accelerated exhumation locally and that is consistent with the overall structural evolution of the Collahuasi district is proposed in the model below.

Rapid exhumation during the early Oligocene unroofed late Eocene shallow-crustal magma chambers. The reduction in confining pressure caused a switch from lithostatic to hydrostatic pressure and promoted hydrothermal fluid flow. Partial exhumation of the Rosario hydrothermal system caused telescoping of the high-sulfidation epithermal veins onto the earlier formed porphyry-style mineralization and alteration assemblages. The model presented in Figure 22

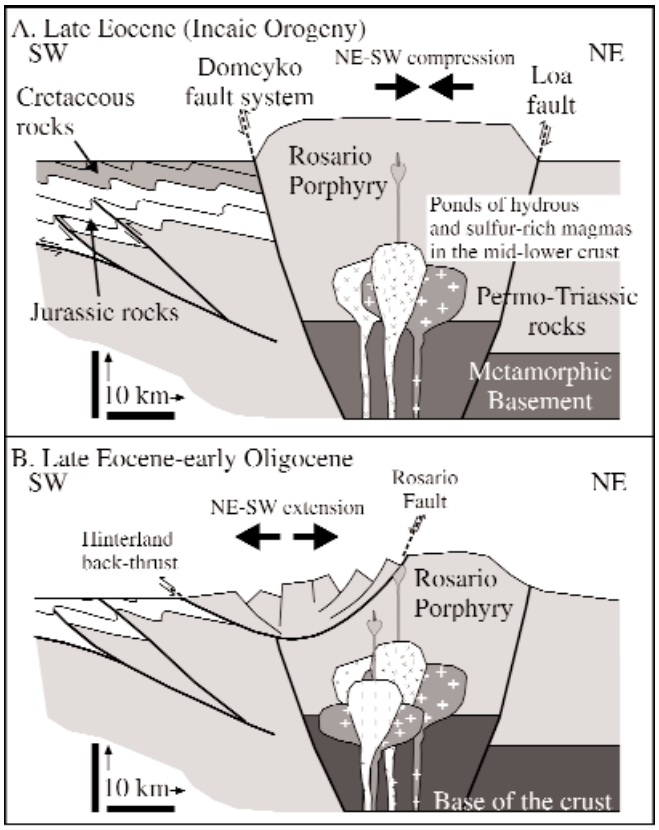


FIG. 22. Northeast-southwest schematic section showing a model of divergent gravitational collapse inferred to have affected the Collahuasi district. A. Most of the late Eocene shortening was accommodated by isoclinal folds in the Mesozoic sedimentary and volcanic rocks. Note that the Permian basement was uplifted relative to the Mesozoic sequences along deep structures, which may have included the Domeyko and Loa fault systems. Thin-skinned deformation (e.g., reverse faults) was accommodated along low-angle thrusts and inverted basin-margin faults. Magmas ascended from a mixing, assimilation, storage, and homogenization (MASH) zone at the base of the crust to levels of neutral buoyancy in the middle-to-upper crust. They did not erupt but crystallized and produced high-level, intrusion-centered brittle-ductile veins (e.g., the early-stage veins at Rosario). B. Partial collapse of the orogenic belt is inferred to have occurred at the end of the Incaic orogeny. Crustal units were detached along gravity slides that were potentially connected to thrusts in the foreland. Detritus from erosion was either collected in basins above the detachments or transported out of the system. Exhumation changed the environment from lithostatic to hydrostatic at the site of ore formation and coincided with formation of intermediate- and late-stage veins at Rosario. That porphyry and superimposed high-sulfidation style mineralization occur at the same crustal level implies protracted intrusive activity at Rosario and the existence of a well-developed and replenished MASH zone at the base of the crust. Adapted for the Collahuasi district from a diagram in Rey et al. (2001).

incorporates the conditions of fixed boundary gravitational collapse (e.g., Rey et al., 2001). Tectonic relaxation and magma intrusion at the end of a major orogeny can be accompanied by propagation of normal faults (Fig. 22; Vanderhaeghe and Teyssier, 2001). Gravitational sliding occurs in the brittle crust on divergent faults that transport the upper crustal units away from the uplifted lithosphere. These normal faults can be high angle in the upper crust and merge into low-angle detachment zones near the brittle-ductile transition (Vanderhaeghe and Teyssier, 2001) or connect to thrusts in the foreland and hinterland (Rey et al., 2001). Detritus produced by erosion was either transported away or may have accumulated in basins above the detachments. An example of a synmineralization debris flow in the region may be the Sichal Formation (Marinovic and Lahsen, 1984), which was deposited in intermontane basins during the late Eocene to Oligocene.

Reconstruction of convergence vectors along the South American continental margin has shown that at the time of porphyry ore formation in late Eocene-early Oligocene, subduction was east-northeast directed (Pardo-Casas and Molnar, 1987). The overall pattern of shortening in the Collahuasi district is consistent with this direction of convergence. However, syn- and postmineralization normal and strike-slip movement in the northwest- and north-northeast–trending faults at Rosario are associated with a local stress field not readily reconciled with that expected for the far field stresses. If the regional stress field remained constant during this period, then normal fault development at Rosario may have reflected decoupling of upper and lower crustal stresses (e.g., gravitational collapse at the end of an orogenic event). Alternatively, there may have been a fundamental change in lithospheric stress, possibly related to a transient change in the convergence direction, rate of subduction, or trench blockages (Richards, 2000).

Two main tectonic models have been advanced to explain the spatial and temporal emplacement of the cluster of world-class porphyry copper deposits along the Domeyko fault system. The first model proposes that transtensional deformation in the arc-parallel fault system favored emplacement of epizonal intrusions associated with copper mineralization (e.g., Lindsay et al., 1995; Reutter et al., 1996; Dilles et al., 1997; Tomlinson and Blanco, 1997a, b). The second model advocates the trapping of magmas related to porphyry Cu mineralization at structural sites along inverted back-arc basin faults (McClay et al., 2002) and may best explain the geologic features observed in the Collahuasi district. Both models are consistent with the northeast-directed convergence determined for the Andean margin during the late Eocene-early Oligocene (Pardo-Casas and Molnar, 1987). However, subduction-coupled rock uplift also requires synchronous erosion to account for rapid exhumation (England and Molnar, 1990). In the Collahuasi district, Permo-Triassic crystalline basement, uplifted relative to the Jurassic and Cretaceous sedimentary rocks, provided the structural trap for ore-related magmas, and porphyry and epithermal ore formation postdates the Incaic orogeny (Pardo-Casas and Molnar, 1987). A model of gravitational collapse is consistent with the estimated convergence rates, which were slower in this period than during the Incaic orogeny (Pardo-Casas and Molnar, 1987). We infer that shallow-crustal extension following rapid convergence and crustal thickening has been a critical element in the formation of high-sulfidation ore in the porphyry deposits of northern Chile, as it facilitated shallow-crustal fluid flow during the transition from lithostatic to hydrostatic pressure.

### *Implications for exploration*

Cooling and collapse of the Rosario hydrothermal system implies emplacement of a second blind intrusion, somewhere beneath Rosario and Cerro La Grande, in order to account for the later high-sulfidation vein systems. Precious metal zoning

at the district scale, together with the overall fault geometries (Fig. 21D), suggests that this rejuvenated magmatic activity was focused between Cerro La Grande and Rosario. Exploration for additional copper resources in the Rosario area should thus be guided by the distribution of the phyllic assemblage beneath Cerro La Grande, as this alteration represents the root zone of the epithermal system and potentially occurs at the top of an as yet undrilled porphyry-style ore deposit. Given the discovery of copper-molybdenite skarn mineralization on the northeast side of the Rosario Porphyry, there may also be potential for distal base metal (Zn, Pb) and/or precious metal (Au, Ag) carbonate-hosted deposits.

Reconnaissance short wave infrared (SWIR) spectroscopy has identified phyllosilicate assemblages (muscovite, illite, ±smectite, ±chlorite) in the hydrothermally altered rocks at Rosario and La Grande. The presence of muscovite may indicate lateral proximity to advanced argillic alteration, potentially associated with massive sulfide veins. Alternatively, muscovite may occur in the vertical transition between the epithermal and porphyry environments (e.g., Lepanto-FSE: Hedenquist et al., 1998). Illite occurs with or without chlorite in the weakly mineralized assemblage that is the latest stage of porphyry-style alteration and mineralization at Rosario. However, illite is also present in an assemblage with smectite, distal from advanced argillic alteration that surrounds massive sulfide veins. The presence of illite ± chlorite may therefore indicate proximity to porphyry-style mineralization in the Collahuasi district, whereas the assemblage illite-smectite may be the outer zone of alteration related to high-level epithermal veins.

## Acknowledgments

This study was completed as a part of the senior author's Ph.D. dissertation at the University of Tasmania. The work was also part of Australian Mineral Industry Research Association (AMIRA) International project P511. We are grateful to the Centre for Ore Deposit Research (CODES) Special Research Centre, AMIRA International, CSIRO Exploration and Mining and Compañia Minera Doña Inés de Collahuasi (CMDIC) for providing financial, logistical, and technical support. Manuel Durán is thanked for approving and funding the work at Collahuasi. We appreciate permission to publish from AMIRA International and CMDIC.

*November 24, 2004; July 5, 2005*

## REFERENCES

Ayllon, F., Bakker, R.J., and Warr, L.N., 2003, Re-equilibration of fluid inclusions in diagenetic-anchizonal rocks of the Cinera-Matallana coal basin (NW Spain): Geofluids, v. 3, p. 49–68.

Arancibia, O.N., and Clark, A.H., 1996, Early magnetite-amphibole-plagioclase alteration-mineralization in the Island Copper porphyry copper-gold-molybdenum deposit, British Columbia: Economic Geology, v. 91, p. 402–438.

Arribas, A., Jr., 1995, Characteristics of high-sulfidation epithermal deposits, and their relation to magmatic fluid: Mineralogical Association of Canada Short Course Series, v. 23, p. 419–454.

Arribas, A. Jr., Hedenquist, J.W., Itaya, T., Okada, T., Concepcion, R.A., and Garcia, J.S.J., 1995, Contemporaneous formation of adjacent porphyry and epithermal Cu-Au deposits over 3000 Ka in northern Luzon, Philippines: Geology, v. 23, p. 337–340.

Audetát, A., and Günther, D., 1999, Mobility and $H_2O$ loss from inclusions in natural quartz crystals: Contributions to Mineralogy and Petrology, v. 137, p. 1–14.

Bloom, M.S., 1981, Chemistry of inclusion fluids: Stockwork molybdenum deposits from Questa, New Mexico, and Hudson Bay Mountain and Endako, British Columbia: Economic Geology, v. 76, p. 1906–1920.

Bodnar, R.J., 1994, Synthetic fluid inclusions XII. Experimental determinations of the liquidus and isochores for a 40 wt. % $H_2O$-NaCl solution: Geochimica et Cosmochimica Acta, v. 55, p. 1053–1063.

Bodnar, R.J., and Beane, R.E., 1980, Temporal and spatial variations in hydrothermal fluid characteristics during vein filling in pre-ore cover overlying deeply buried porphyry copper-type mineralization at Red Mountain, Arizona: Economic Geology, v. 75, p. 876–893.

Bodnar, R.J., Burnham, C.W., and Sterner, S.M., 1985, Synthetic fluid inclusions in natural quartz. III. Determination of phase equilibrium properties in the system $H_2O$–NaCl to 1000ºC and 1500 bars: Geochimica et Cosmochimica Acta, v. 49, p. 1861–1873.

Bodnar, R.J., Sterner, S.M., and Hall, D.L., 1989, SALTY: A FORTRAN program to calculate compositions of fluid inclusions in the system NaCl-KCl-$H_2O$: Computers and Geosciences, v. 15, p. 19–41.

Clark, A.H., Archibald, D.A., Lee, A.W., Farra, E., and Hodgson, C.J., 1998, Laser probe $^{40}Ar/^{39}Ar$ ages of early- and late-stage alteration assemblages, Rosario porphyry copper-molybdenum deposit, Collahuasi district, I region, Chile.: Economic Geology, v. 93, p. 326–337.

Cline, J.S., and Bodnar, R.J., 1994, Direct evolution of brine from a crystallizing silicic melt at Questa, New Mexico, molybdenum deposit: Economic Geology, v. 89, p. 1780–1802.

Cline, J.S., and Vanko, D.A., 1995, Magmatically generated saline brines related to molybdenum at Questa, New Mexico, USA: Mineralogical Association of Canada Short Course Series, v. 23, p. 153–174.

Cooke, D.R., and Simmons, S.F., 2000, Characteristics and genesis of epithermal gold deposits: Reviews in Economic Geology v. 13, p. 221–244.

Dick, L.A., Chavez, W.X., Gonzales, A., and Bisso, C., 1994, Geologic setting and mineralogy of the Cu-Ag-(As) Rosario vein system, Collahuasi district, Chile: Society of Economic Geologists Newsletter, no. 19, p. 1, 6–11.

Dilles, J.H., and Einaudi, M.T., 1992, Wall-rock alteration and hydrothermal flow paths about the Ann-Mason porphyry copper deposit, Nevada—a 6-km vertical reconstruction: Economic Geology, v. 87, p. 1963–2001.

Dilles, J.H., Tomlinson, A.J., Martin, M.W., and Blanco, N., 1997, El Abra and Fortuna complexes: A porphyry copper batholith sinistrally displaced by the Falla Oeste: Congreso Geológico Chileno, VIII, Antofagasta, Chile, Proceedings, p. 1883–1887.

Doblas, M., 1998, Slickenside kinematic indicators: Tectonophysics, v. 295, p. 187–197.

Eastoe, C.J., 1978, A fluid inclusion study of the Panguna porphyry copper deposit, Bougainville, Papua New Guinea: Economic Geology, v. 73, p. 721–748.

——1982, Physics and chemistry of the hydrothermal system at the Panguna porphyry copper deposit, Bougainville, Papua New Guinea: Economic Geology, v. 77, p. 127–153.

Etchecopar, A., Vasseur, G., and Gaignieres, M., 1981, An inverse problem in microtectonics for the determination of stress tensors from fault striation analysis: Journal of Structural Geology, v. 3, p. 51–65.

England, P., and Molnar, P., 1990, Surface uplift, uplift of rocks, and exhumation of rocks: Geology, v. 18, p. 1173–1177.

Fournier, R.O., 1987, Conceptual models of brine evolution in magmatic-hydrothermal systems: U.S. Geological Survey Professional Paper 1350, p. 1487–1506.

——1991, Transition from hydrostatic to greater than hydrostatic fluid pressure in presently active hydrothermal systems in crystalline rocks: Geophysical Research Letters, v. 18, p. 955–958.

——1999, Hydrothermal processes related to movement of fluid from plastic rock into brittle rock in the magmatic-epithermal environment: Economic Geology, v. 94, p. 1193–1211.

Gustafson, L.B., and Hunt, J.P., 1975, The porphyry copper deposit at El Salvador, Chile: Economic Geology, v. 70, p. 857–912.

Haas, J.L., Jr., 1971, The effect of salinity on the maxim thermal gradient of a hydrothermal system at hydrostatic pressure: Economic Geology, v. 66, p. 940–946.

Hedenquist, J.W., 1987, Volcanic-related hydrothermal systems in the Circum-Pacific basin and their potential for mineralization: Mining Geology, v. 37, p. 347–364.

Hedenquist, J.W., and Henley, R.W., 1985, The importance of $CO_2$ on freezing point measurements of fluid inclusions: Evidence from active geothermal systems and implications for epithermal ore deposition: Economic Geology, v. 80, p. 1379–1406.

Hedenquist, J.W., Arribas, A., and Reynolds, T.J., 1998, Evolution of an intrusion-centered hydrothermal system: Far Southeast Lepanto porphyry and epithermal Cu-Au deposits, Philippines: Economic Geology, v. 93, p. 374–404.

Heinrich, C.A., 2003, Magmatic vapor condensation and the relation between porphyries and epithermal Au(Cu-As) mineralization: Thermodynamic constraints: Mineral Exploration and Sustainable Development, Society for Geology Applied to Mineral Deposits Biennial Meeting, 7th, Proceedings, v. 1, p. 279–282.

Hemley, J.J., 1959, Some mineralogical equilibria in the system $K_2O$-$Al_2O_3$-$SiO_2$-$H_2O$: American Journal of Science, v. 257, p. 241–270.

Hunt, J.P., Bratt, J.A., and Marquardt, L., 1983, Quebrada Blanca, Chile: An enriched porphyry copper deposit: Mining Engineering, v. 35, p. 636–644.

Jackson, J.A., and White, N.J., 1989, Normal faulting in the upper continental crust: Observations from regions of active extension: Journal of Structural Geology, v. 11, p. 15–36.

Kontak, D.J., and Clark, A.H., 2002, Genesis of the giant, bonanza San Rafael lode tin deposit, Perú: Origin and significance of pervasive alteration: Economic Geology, v. 97, p. 1741–1777.

Lee, A.W., 1994, Evolution of the Rosario copper-molybdenum porphyry deposit and associated copper-silver vein system, Collahuasi district, I region, northern Chile: Unpublished M.A. thesis, Kingston, Ontario, Canada, Queens University, 75 p.

Lindsay, D.D., Zentilli, M., and Rojas De La Rivera, J., 1995, Evolution of an active ductile to brittle shear system controlling mineralization at the Chuquicamata porphyry copper deposit, northern Chile: International Geology Reviews, v. 37, p. 945–958.

Losada-Calderon, A.J., 1992, Geology and geochemistry of Nevados del Famatina and La Mejicana deposits, La Rioja province, Argentina: Unpublished Ph.D. thesis, Melbourne, Australia, Monash University, 320 p.

Losada-Calderon, A.J., McBride, S.L., and McPhail, D.C., 1994, The geology and $^{40}Ar/^{39}Ar$ geochronology of magmatic activity and related mineralization in the Nevados Famatina mining district, La Rioja province, Argentina: Journal of South American Earth Sciences, v. 7, p. 9–24.

Maksaev, V., 1990, Metallogeny, geological evolution, and thermochronology of the Chilean Andes between latitudes 21° and 26° South, and the origin of major porphyry copper deposits: Unpublished Ph.D. thesis, Halifax, Canada, Dalhousie University, 554 p.

Maksaev, V., and Zentilli, M., 2000, Fission track thermochronology of the Domeyko Cordillera, northern Chile: Implications for Andean tectonics and porphyry copper metallogenesis: Exploration and Mining Geology, v. 8, p. 65–89.

Marinović, N., and Lahsen, A., 1984, Hoja Calama. Carta Geológica de Chile, Escala 1:250,000: Servicio Nacional de Geología y Minería, p. 58.

Masterman, G.J., 2003, Structural and geochemical evolution of the Rosario Cu-Mo porphyry deposit and related Cu-Ag veins, Collahuasi district, northern Chile: Unpublished Ph.D. thesis, Tasmania, Australia, University of Tasmania, 253 p.

Masterman, G.J., Cooke, D.R., Berry, R.F., Clark, A.H., Archibald, D.A., Mathur, R., Walshe, J.L., and Duran, M., 2004, $^{40}Ar/^{39}Ar$ and Re-Os geochronology of porphyry copper-molybdenum deposits and related copper-silver veins in the Collahuasi district, northern Chile: Economic Geology, v. 99, p. 673–690.

McClay, K., Skarmeta, J., and Bertens, A., 2002, Structural controls on porphyry copper deposits in northern Chile, *in* Swager, C.P., Stone, B., and Reddy, S., New models and implications for Cu-Mo mineralization in subduction orogens: Australian Institute of Geologists, Applied Structural Geology for Mineral Exploration and Mining, Kalgoorlie, Western Australia, 2002, Extended Abstracts, p. 127.

Moore, R.L., and Masterman, G.J., 2002, The geology and corporate discovery history of the Collahuasi district porphyry copper deposits, Chile: Hobart, Australia, University of Tasmania, Centre for Ore Deposit Research Special Publication 4, p. 23–50.

Nash, J.T., 1976, Fluid inclusion petrography—data from porphyry copper deposits and application to exploration: U.S. Geological Survey, Professional Paper 907D, 16 p.

——2001, Porphyry-epithermal transition: Maricunga belt, northern Chile: Economic Geology, v. 96, p. 743–772.

Ossandon, C.G., Freraut, C.R., Gustafson, L.B., Lindsay, D.D., and Zentilli, M., 2001, Geology of the Chuquicamata mine: A progress report: Economic Geology, v. 96, p. 249–270.

Padilla Garza, R.A., Titley, S.R., and Pimentel B., F., 2001, Geology of the Escondida porphyry copper deposit, Antofagasta region, Chile: Economic Geology, v. 96, p. 307–324.

Pardo-Casas, F., and Molnar, P., 1987, Relative motion of the Nazca (Farallón) and South American plates since Late Cretaceous time: Tectonics, v. 6, p. 233–248.

Petit, J.P., 1987, Criteria for sense of movement on fault surfaces in brittle rocks: Journal of Structural Geology, v. 9, p. 597–608.

Pitzer, K.S., and Pabalan, R.T., 1986, Thermodynamics of NaCl in steam: Geochimica et Cosmochimica, v. 50, p. 1445–1454.

Platt, J., 1988, La Grande vein project exploration proposal: Santiago, Compañia Minera Doña Inés de Collahuasi, internal company report, 13 p.

Potter, R.W., Clynne, M.A., and Brown, D.L., 1978, Freezing point depressions of aqueous sodium chloride solutions: Economic Geology, v. 73, p. 284–285.

Reutter, K.J., Scheuber, E., and Chong, G., 1996, The Precordilleran fault system of Chuquicamata, northern Chile: Evidence for reversals along arc-parallel strike-slip faults: Tectonophysics, v. 259, p. 213–228.

Rey, P., Vanderhaeghe, O., and Teyssier, C., 2001, Gravitational collapse on the continental crust and flow of orogens: Tectonophysics, v. 342, p. 435–449.

Reyes, A.G., 1990, Petrology of Philippine geothermal systems and the application of alteration mineralogy to their assessment: Journal of Volcanology and Geothermal Research, v. 43, p. 279–309.

Richards, J.P., 2000, Lineaments revisited: Society of Economic Geologists Newsletter 42, p. 1, 14–20.

Richards, J.P., and Kerrich, R., 1993, The Porgera gold mine, Papua New Guinea: Magmatic hydrothermal to epithermal evolution of an alkalic precious metal deposit: Economic Geology, v. 88, p. 1017–1052.

Roedder, E., 1984, Fluid inclusions: Reviews in Mineralogy, v. 12, 644 p.

Roedder, E., and Bodnar, R.J., 1980, Geologic pressure determinations from fluid inclusion studies: Annual Reviews in Earth and Planetary Sciences, v. 8, p. 263–301.

Sibson, R.H., 2001, Seismogenic framework for hydrothermal transport and ore deposition: Reviews in Economic Geology, v. 14, p. 25–50.

Sillitoe, R.H., 2000, Styles of high-sulfidation gold, silver and copper mineralization in porphyry and epithermal environments: Australian Institute of Mining and Metallurgy, PacRim '99, Bali, Indonesia, 10–13 October, Proceedings, p. 29–44.

Sillitoe, R.H., Marquardt, J.C., Ramirez, F., Becerra, H., and Gomez, M., 1996, Geology of the concealed MM porphyry copper deposit, Chuquicamata district, northern Chile: Society of Economic Geologists Special Publication 5, p. 59–70.

Sterner, S.M., Hall, D.L., and Bodnar, R.J., 1988, Synthetic fluid inclusions. V. Solubility relations in the system NaCl-KCl-$H_2O$ under vapor-saturated conditions: Geochimica et Cosmochimica Acta, v. 52, p. 989–1005.

Sverjensky, D.A., Hemley, J.J., and D'Angelo, W.M., 1991, Thermodynamic assessment of hydrothermal alkali feldspar-mica-alumnosilicate equilibria: Geochimica et Cosmochimica Acta, v. 55, p. 989–1004.

Thompson, A.J.B., Hauff, P.L., and Robitalle, A.J., 1999, Alteration mapping in exploration: Application of short-wave infrared (SWIR) spectroscopy: Society of Economic Geologists Newsletter 39, p. 1, 16–17.

Tomlinson, A.J., and Blanco, N., 1997a, Structural evolution and displacement history of the West fault system, Precordillera, Chile: Part 1. Synmineral history: Congreso Geológico Chileno, VIII, Antofagasta, Chile, 1997, Proceedings, p. 1873–1877.

——1997b, Structural evolution and displacement history of the West fault system, Precordillera, Chile: Part 2. Postmineral history: Congreso Geológico Chileno, VIII, Antofagasta, Chile, 1997, Proceedings, p. 1878–1882.

Vanderhaeghe, O., and Teyssier, C., 2001, Crustal-scale rheological transitions during late orogenic collapse: Tectonophysics, v. 335, p. 211–228.

Vergara, H.L., and Thomas, A.N., 1984, Hoja Collacagua, Región de Tarapacá, Carta Geológica de Chile, Escala 1:250,000: Santiago, Servicio Nacional de Geología y Minería, p. 79.

White, N.C., and Hedenquist, J.W., 1990, Epithermal environments and styles of mineralization: Variations and their causes, and guidelines for exploration: Journal of Geochemical Exploration, v. 36, p. 445–474.

——1995, Epithermal gold deposits: Styles, characteristics and exploration: Society of Economic Geologists Newsletter 23, p. 1, 9–13.